aerospace

MDPI

Article

Analysis of the Aeroacoustic Characteristics of a Rigid Coaxial Rotor in Forward Flight Based on the CFD/VVPM Hybrid Method

Yucheng Yang, Guohua Xu *, Yongjie Shi and Zhiyuan Hu

National Key Laboratory of Rotorcraft Aeromechanics, Nanjing University of Aeronautics and Astronautics, Nanjing 210016, China; yangyucheng93@nuaa.edu.cn (Y.Y.); shiyongjie@nuaa.edu.cn (Y.S.); huzhiyuan@nuaa.edu.cn (Z.H.)

* Correspondence: ghxu@nuaa.edu.cn

Abstract: This study develops a hybrid solver with reversed overset assembly technology (ROAT), a viscous vortex particle method (VVPM), and a CFD program based on the URNS method, in order to study the aerodynamic and acoustic characteristics of coaxial rigid rotors. The aerodynamic load of the "AH-1G" helicopter rotor is first calculated based on the hybrid method and compared with available experimental data. The prediction of the linear noise of the OLS rotor is then performed and the obtained results are compared with available experimental data. These results allow the evaluation of the accuracy of the hybrid method for emulating rotor aerodynamics and acoustics. Afterwards, the hybrid and CFD methods are applied to obtain the aerodynamic and acoustic characteristics of the given coaxial rigid rotor model, while taking into account the trim of the collective pitch. The obtained results demonstrate that the hybrid method has high proficiency in capturing blade–vortex-interaction impulsive loads and high computational efficiency in predicting associated loading noise characteristics. Furthermore, the effect of the hybrid method on the noise characteristics of coaxial rigid rotors under a different advance ratio, blade tip speed, shaft angle, and other conditions, as well as the impact of the upper and lower rotors on the noise contribution of the coaxial rotor are analyzed. Finally, the impacts of the initial phase and the vertical spacing on the sound pressure level are studied.

Keywords: rigid coaxial rotor; aerodynamic acoustics; initial azimuth; hybrid method; VVPM method

check for updates

Citation: Yang, Y.; Xu, G.; Shi, Y.; Hu, Z. Analysis of the Aeroacoustic Characteristics of a Rigid Coaxial Rotor in Forward Flight Based on the CFD/VVPM Hybrid Method. *Aerospace* **2024**, *11*, 21. https://doi.org/10.3390/aerospace11010021

Received: 20 November 2023
Revised: 21 December 2023
Accepted: 22 December 2023
Published: 26 December 2023

Copyright: © 2023 by the authors. Licensee MDPI, Basel, Switzerland. This article is an open access article distributed under the terms and conditions of the Creative Commons Attribution (CC BY) license (https://creativecommons.org/licenses/by/4.0/).

1. Introduction

In several studies on the analysis of the aerodynamic and noise characteristics of rigid coaxial rotors, tools were developed to predict their aerodynamic loads and noise. For instance, Jia et al. [1–3] used the RCAS Helios tool and the PSU-WOPWOP noise program to perform aerodynamic and noise analysis of high-speed coaxial helicopters under different working conditions. They also studied the grid resolution and calculation accuracy of turbulence models. Zhu [4] and Wang et al. [5] utilized a URANS-based CFD approach and the FW-Hpds equations to predict the aerodynamic noise characteristics of coaxial rotors in hovering and forward flight configurations. In addition, they subsequently conducted analyses on the propagation properties of high-speed impulsive (HSI) noise.

Some researchers also used vortex methods to simulate the rotor wake interference effects. For instance, Singh [6] used the VVPM method coupled with an aeroelastic model to conduct a study on the aerodynamic characteristics of coaxial rotors in hover and forward flight states. Based on the free-wake method and the PSU-WOPWOP program [7], Sharma [8] considered a wider range of state parameters and conducted aerodynamic and acoustic analyses on the XH-59A rigid coaxial rotor. He studied the parametric laws of high-speed, rigid-body, blade–vortex interaction (BVI) events in coaxial rotors. Based on the vorticity transport model (VTM) method developed by Brown [9,10], Kim [11] studied the

impacts of the lift offset and rotor hub stiffness on the noise characteristics of coaxial rotors, and compared them with the noise characteristics of equivalent single rotors [12]. However, the CFD methods cannot avoid the unphysical numerical diffusion of rotor wake vortices when applied to rotor flow field calculations, and they require significant computational resources. On the other hand, the vortex methods have high computational efficiency, but cannot accurately simulate the nonlinear flow features of the near-body flow field of the blades. Therefore, this paper proposes a novel CFD/VVPM hybrid method to balance the computational efficiency and accuracy for the calculation of the aerodynamics and acoustics of rigid coaxial rotors.

Researchers have proposed and tried to apply the hybrid methods for rotor aerodynamic and acoustic prediction. Egolf et al. [13] employed a coupled CFD/vortex approach for noise prediction in forward flight states. In this method, the vortex wake model is established on a Lagrangian framework consisting of discrete, piecewise, linear, geometric constituents endowed with bound and trailing vortex elements exhibiting constant circulation intensities. Zhao et al. [14] proposed a CFD/VVPM hybrid method combining the OVERFLOW CFD code. Based on the latter approach, Rajmohan [15] studied and validated the aerodynamic characteristics of coaxial rotors in hover. On the contrary, few studies have been conducted on the numerical simulation of the flow field and acoustic characteristics of coaxial rotors in forward flight. Therefore, the proposed hybrid method focuses on the analysis of the aerodynamic and acoustic characteristics of rigid coaxial rotors in forward flight.

To effectively predict the rotor aerodynamic and acoustic characteristics, high-fidelity simulation methods that account for pitch inputs are required. A single rotor only requires three control inputs, while coaxial rotors require the consideration of six pitch inputs of the upper and lower rotor. Moreover, the strong aerodynamic interactions between the rotors leads to more complex trim balancing. In the study presented in [16] the trim of coaxial rotors in hover was conducted to meet the requirements of studying the aerodynamic interaction characteristics. For the forward flight condition, this study develops a coaxial rigid rotor trim methodology based on the "differential method" to satisfy the requirements of high-fidelity simulations.

Due to the compact structure and small inter-rotor spacing of the coaxial rigid rotors, the upper and lower rotor blade grids used in the numerical simulations interfere with each other. In the study presented in [16], sliding mesh methods were used for the rotation of the upper and lower rotors to avoid this issue. However, this is not well-suited for the numerical computation in forward flight conditions. This study applies the previously developed ROAT technique [17] to the blade grids, which can avoid the interpolation cell orphaning issue [18] and the discontinuous hole boundary cell issue caused by the failure in finding contributing cells.

By applying the established CFD/VVPM hybrid method, this study conducts an analysis on the aerodynamic and acoustic characteristics of coaxial rigid rotors under forward flight conditions. The effects of the rotor spacing, initial azimuth angle, forward flight velocity, and other parameters are also studied. The obtained results demonstrate that at the higher blade tip speed, the upper rotor is mainly affected by the blade–vortex interaction, which leads to periodic variations in the loading noise distribution on the observer plane. On the contrary, the lower rotor is mainly affected by rotor–wake interactions, which results in loading noise distributions analogous to a single rotor.

2. Computational Methodology and Performance Assessment

The Farassat 1A formula [19], which is widely used in studies on the aerodynamic noise of rotating blades, such as aircraft propellers and rotors, is applied to calculate the rotor acoustic characteristics, as shown in Equation (1). The first and second terms in this equation correspond to the thickness noise and loading noise, respectively. This study uses the same methodology for acoustic analysis. At a high advance ratio during forward flight, the blade tip Mach number at the advance side is high, which generates nonlinear

quadrupole noise. The source surface in the Farassat1A formula uses the blade surface, which only includes the rotational noise of the rotor, that is, the thickness noise related to the thickness of the blade and rotational velocity, and loading noise related to unsteady loads of the blade.

$$\begin{aligned} 4\pi p'_T(x,t) &= \int_{f=0} \left[\frac{\rho_0(v_n+v_n)}{r(1-M_r)^2}\right]_{ret} dS + \int_{f=0} \left[\frac{\rho_0 v_n(rM_r+c_0(M_r-M^2))}{r^2(1-M_r)^3}\right]_{ret} dS \\ 4\pi p'_L(x,t) &= \frac{1}{c_0}\int_{f=0} \left[\frac{l_r}{r(1-M_r)^2}\right]_{ret} dS + \int_{f=0} \left[\frac{l_r-l_M}{r^2(1-M_r)^2}\right]_{ret} dS \\ &+\frac{1}{c_0}\int_{f=0} \left[\frac{l_r(rM_r+c_0(M_r-M^2))}{r^2(1-M_r)^3}\right]_{ret} dS \end{aligned} \quad (1)$$

The load of the rotors is obtained through the simulation of their flow field using the VVPM/CFD method. The near-blade flow field adopts an unsteady Reynolds-averaged Navier–Stokes (uRANS) method based on Eulerian grids, which is implemented through the RADAS CFD solver [17]. The latter is a non-structured CFD solver for compressible-viscous-flow numerical simulation, suitable for simulating the nonlinear characteristics of compressible viscous flow and near-wake effects in the near-blade flow field. Its accuracy has been validated in many studies on rotor aerodynamic and acoustic characteristics [20,21]. In the region far from the blades, the VVPM method based on the meshless Lagrangian description is used to simulate the rotor wake, where the governing equations are the velocity–vorticity form of the incompressible Navier–Stokes equations for solving the wake evolution.

Figure 1 illustrates the coupling process of different modules in the proposed CFD/VVPM method. It can be seen that the flow field of the rotor grids is solved by the CFD block, with blade-surface circumferential load distributions converted to vortex sources and considered as inputs to the VVPM block. The influence of the VVPM wake on the CFD domain is taken into account by imposing induced velocities on each far-field boundary cell of the blade grids [22]. The flow exchange between the upper- and lower-rotor grids uses the ROAT technology, where the Maxhole boundary type performs Chimera interpolation, which is validated in the study presented in [23], as shown in Figure 2a. It can be seen from Figure 2b,c that the ROAT method can accurately perform hole-cutting of the rotor grids and maintain the continuity of zonal interfaces. In addition, the Maxhole interpolation boundaries can reliably capture load variations in coaxial rotors in hover. After obtaining the aerodynamic data using the CFD/VVPM method, the control inputs are trimmed using a differential method to perform collective pitch trimming. Once the trim controls converge, the final loads and noise data are output.

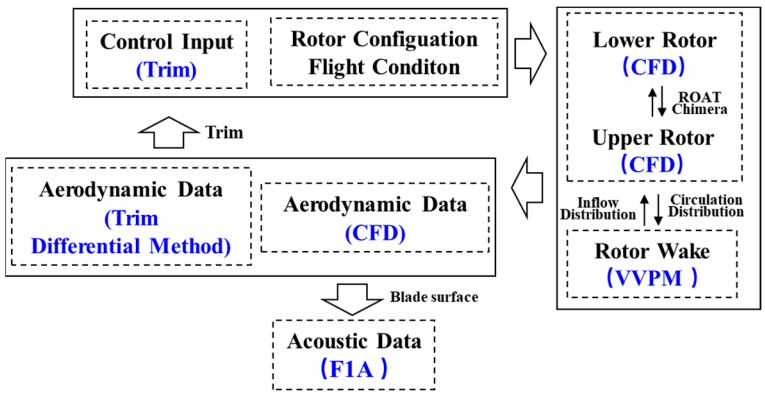
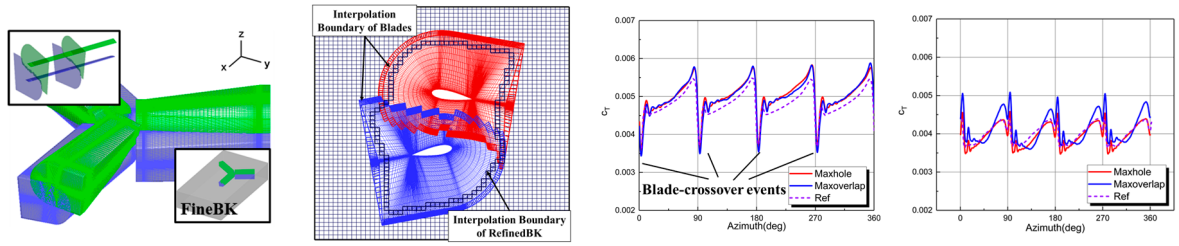


Figure 1. Framework of the Proposed Hybrid Method.



(**a**) Maxhole Boundary (**b**) Maxhole Boundary (**c**) c_T, Upper Rotor (**d**) c_T, Lower Rotor

Figure 2. Chimera Results and Performance of Coaxial Rotors in Hover.

2.1. Rotor Aerodynamic and Aeroacoustics Verification

To evaluate the accuracy of the employed simulation methodology for analysis of the aerodynamic and acoustic characteristics of rotors, the AH1-G helicopter [24] and OLS rotor [25] were chosen for comparison. The same configurations were then adopted for all test cases. More precisely, in the CFD block, the Roe flux scheme is adopted to compute the face fluxes, Green–Gauss cell-centered scheme is used to determine the gradients of the primitive variables, and the Venkatakrishnan limiter is used to prevent the oscillation and divergence in regions with substantial gradients. The one-equation Spalart–Allmaras model [26] was used for RANS closure, and the LUSGS implicit scheme was adopted to progress the transient flow field. A total of 720 time increments per revolution were defined, with a step of 0.5° and 15 sub-iterations per increment. In the VVPM block, the wake can be advanced using larger time steps. An excessive timestep magnitude disparity between the CFD and VVPM domains could reduce the solution accuracy. In this study, a timestep of $\psi = 3°$ was used in the VVPM block.

Moreover, a CFD approach was incorporated for direct comparison with the results obtained by the hybrid method. This CFD methodology uses configurations and rotor grids to those adopted for the implementation of the CFD block of the hybrid method, while adding background grids that are required to simulate the rotor wake.

2.1.1. Aerodynamics of a Single Rotor

The computational conditions for the "AH1-G" helicopter rotor were set as follows: advance ratio of 0.19, blade tip Mach number of 0.65, and thrust coefficient of 0.00464. Table 1 shows the flight test data taken from the studies presented in [24,27] and the trimming results obtained by the hybrid method. It can be observed that the results of the hybrid method are consistent with the computational results of the reference and CFD method, although they all slightly deviate from the flight test measurements. The control angle obtained from the hybrid method has a slightly larger magnitude.

Table 1. Pitch Trimming Results Obtained by Different Approaches.

Pitch Input	Exp	Ref	CFD	Hybrid
$\theta_0/(°)$	6.0	6.1	6.10	6.41
$\theta_{1s}/(°)$	−5.5	−5.1	−5.03	−5.46
$\theta_{1c}/(°)$	1.7	1.3	1.19	1.84

Figure 3 shows the sectional normal force coefficient results obtained by the hybrid and CFD methods, and the experimental data at different radial positions along the rotor azimuth. It can be observed that the computational results obtained by the hybrid and CFD methods are consistent at the cross-sections of 0.75 R and 0.97 R. Around the azimuth of 60°, the hybrid method has more pronounced load fluctuations compared with the CFD method. This coincides with one of the potential rotor–wake interference locations. In addition, minor discrepancies exist between the two computational approaches and the experimental values. This is due to the fact that the calculations do not take into consideration the blade elastic deformations and rotor/fuselage interference effects present in the flight tests.

In summary, the hybrid method has a higher ability to capture blade–vortex interaction fluctuations while preserving a high aerodynamic computational accuracy, compared with the CFD approach.

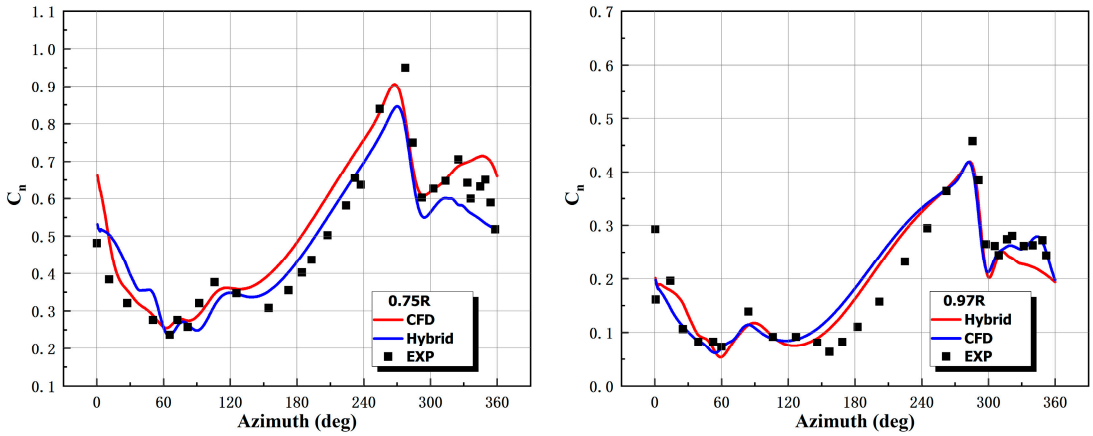


Figure 3. Sectional Normal Force Coefficient of the AH1G Rotor.

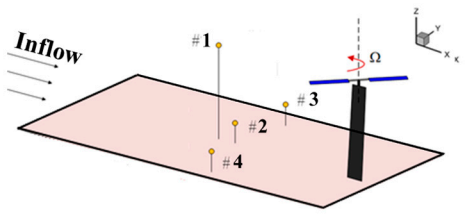
2.1.2. Acoustics of a Single Rotor

The linear noise, including the thickness noise and loading noise, was calculated and validated using the AH-1/OLS model rotor test data. The geometric parameters of the blades used in the calculations are presented in Table 2.

Table 2. Parameters of OLS Rotor.

Radius (m)	Chord (m)	Airfoil	Twist (°/R)	Root (R)	Shape
0.958	0.1039	OLS	−10.0	0.182	Rectangle

The rotor was tested under various conditions in the wind tunnel, providing experimental data for comparison. This study adopts the test condition of 10014 as a typical case exhibiting blade–vortex interaction (BVI) phenomena. A blade tip speed of 0.664 and an advance ratio of 0.164 were used. The blade pitch angle formula is given by $\theta = 6.14 - 0.9\cos\psi - 1.39\sin\psi$, and the flapping angle formula is given by $\beta = 0.5 - 1.0\cos\psi$. The coordinates of the observation points are shown in Figure 4.

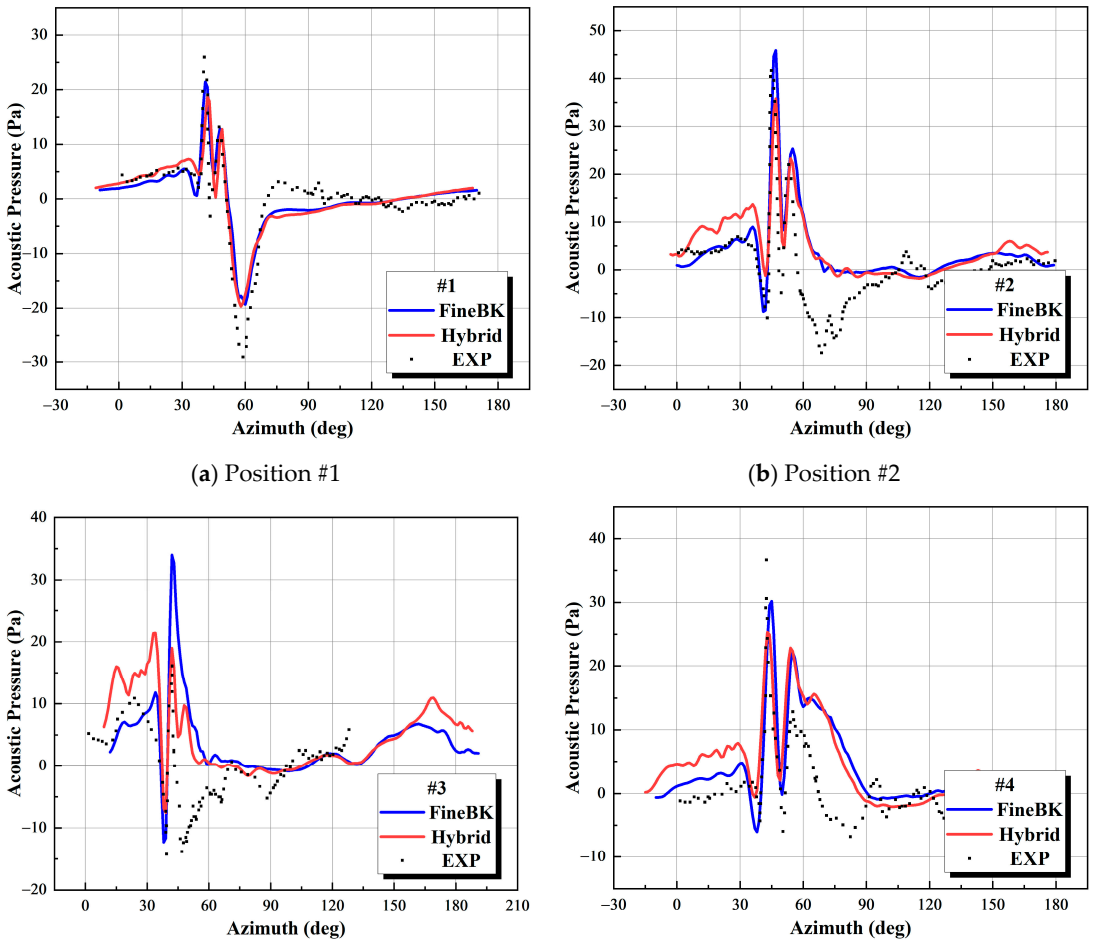


OBS	Coordinate Position
#1	(−3.3, 0.0, 0.0)
#2	(−2.85, 0.0, −1.65)
#3	(−2.47, 1.43, −1.65)
#4	(−2.47, −1.43, −1.65)

Figure 4. Coordinates of Observers.

The acoustic-pressure time histories calculated at the four observation points using the CFD method and hybrid method were compared with the experimental data as shown in Figure 5. At observation point #1, located in the rotor disc plane, the two methods captured fluctuations of two loading noise pulses, one large and one small. At position #3, the fluctuations given by the hybrid method were more consistent with the experimental data. In general, the peaks and fluctuations calculated at each observation point were consistent with the experimental data for the two methods. The observed errors are similar to those of Strawn's [28] BVI noise calculations using CFD methods. This is partially due to the challenge of predicting rotor load fluctuations within the complex vortex interference flow

field under BVI conditions. It is also because the linear noise obtained from calculations based on the F1A formula does not account for the quadrupole noise of the rotor.



(**a**) Position #1 (**b**) Position #2

(**c**) Position #3 (**d**) Position #4

Figure 5. Acoustic-pressure Time History of OLS Rotor.

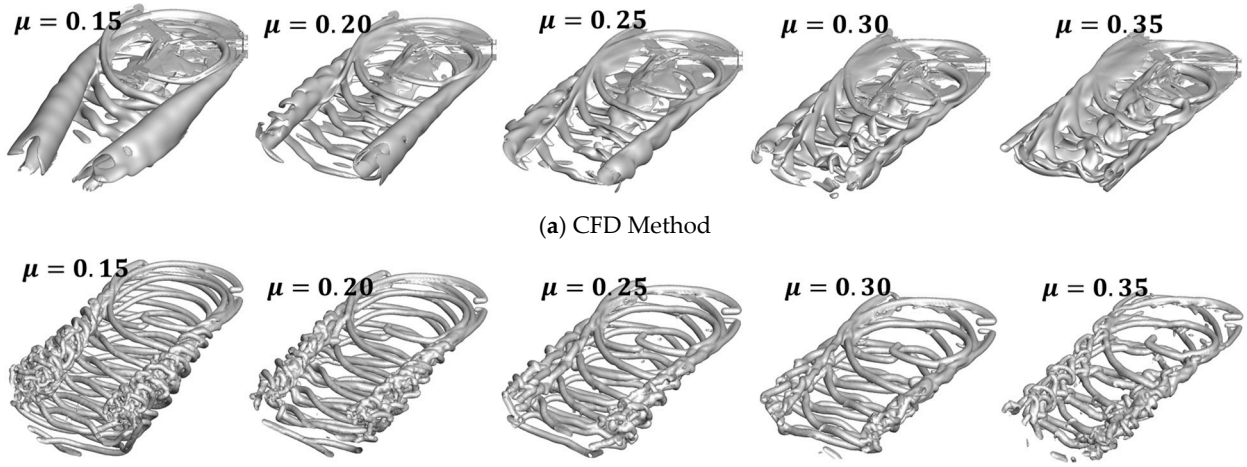
2.2. Comparison of the CFD and Hybrid Methods of a Coaxial Rotor

The examples above verify the high accuracy of the proposed hybrid method for the calculation of the aerodynamic loads and linear noise of single rotors. Compared with single rotors, the more complex disturbance flow characteristics of the flow field of the coaxial rigid rotors increase the simulation difficulty [29]. Consequently, using the Ka-28 coaxial-rotor parameters as a reference, this paper presents a coaxial rotor case to validate the efficiency of the hybrid method for computing the aerodynamic and acoustic characteristics of the coaxial rigid rotor. The parameters are presented in Table 3.

Table 3. Parameters of the Coaxial Rotor.

Parameter	Coaxial Rotor
Rotor Diameter	15.9 m
Chord	0.48 m
Shape	Rectangle
Airfoil	NACA23012
Twist	10°
Tip Velocity (m/s)	220
Num. of Blades	3 + 3

Figure 6 shows the isosurface of the tip vortex of the coaxial rotor at different advance ratios. It can be seen that, compared with the CFD method where the wake dissipates faster, the hybrid method provides clearer features and better preservation of the wake structure. During the backward development of the wake, the tip vortex has strong rolling up at the two outermost positions. Due to the interference and entanglement between the upper- and lower-rotor wakes, the coaxial rotor develops a more complex vortex structure, which relatively flattens out with the increase in the advance ratio. As is shown in the figure, compared to the CFD method, the simulation results of the hybrid method for the characteristics of rotor wake vortices show a clearer vortex structure and do not exhibit non-physical dissipation as the wake develops in the CFD method simulation.



(**a**) CFD Method

(**b**) VVPM Method

Figure 6. Wake Vortex of the Coaxial Rotor with Vorticity Magnitude of 15.

Table 4 shows the rotor pitch obtained by the differential trimming method for the coaxial rotor at an advance ratio (μ) ranging between 0.15 and 0.35 with a V_{tip} of 220 m/s. The coaxial trimming capacity of the CFD program RADAS has been validated in [24]. The differences in pitch angle between the two methods are generally within 0.3°. The small differences between the trimming results indicate that the trimming function of the hybrid method is accurate. The subsequent analyses of the acoustic characteristics of the coaxial rotor under various operating conditions were all performed while completing the trim.

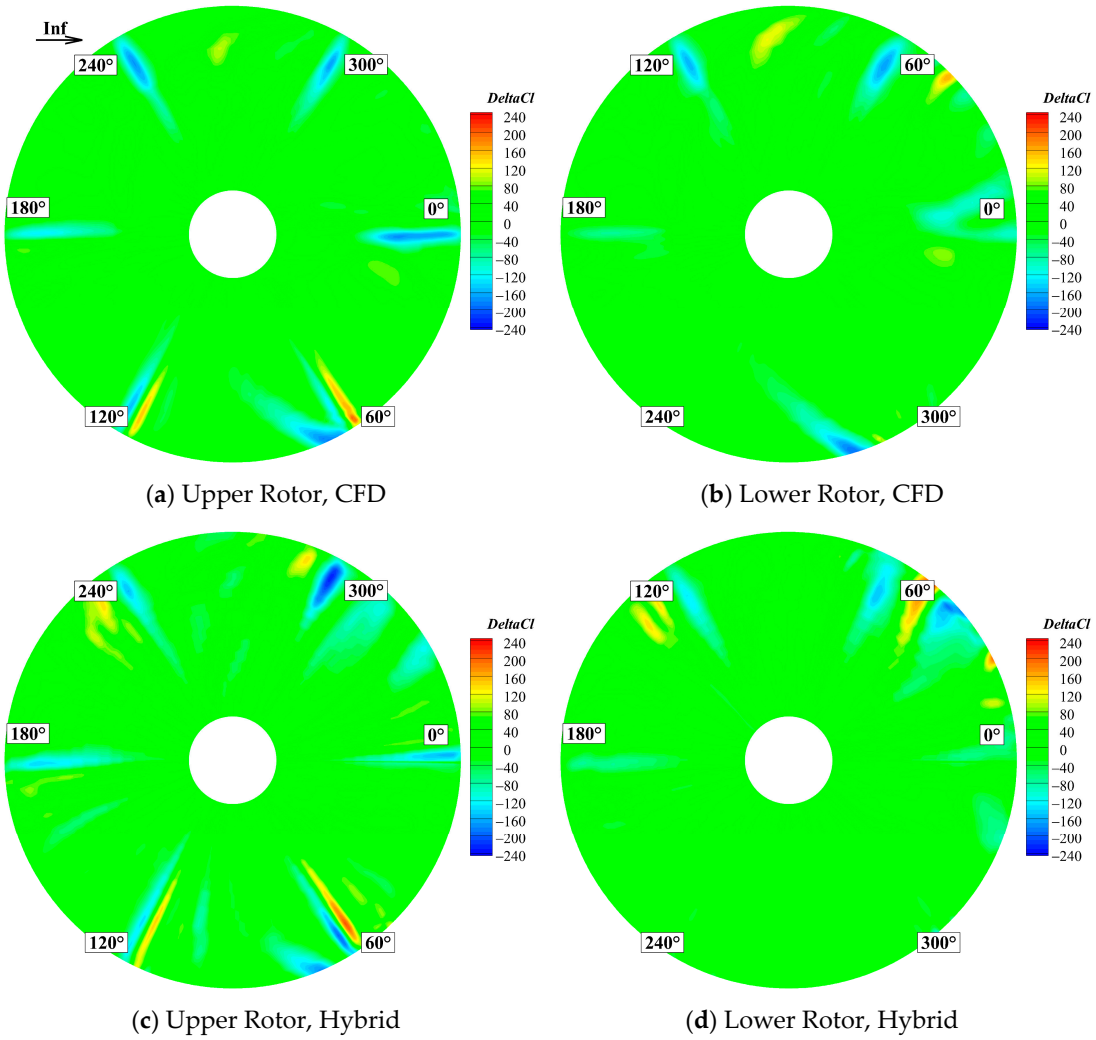
Table 4. Trimmed Blade Pitch Angle of Coaxial Rotor across Advance Ratio.

Advance Ratio	Method	θ_{0upp}/(°)	θ_{1supp}/(°)	θ_{1cupp}/(°)	θ_{0low}/(°)	θ_{1slow}/(°)	θ_{1clow}/(°)
0.15	CFD	8.401	−3.551	3.01	8.352	−3.166	3.020
	Hybrid	8.515	−3.560	2.354	8.409	−3.330	3.004
0.20	CFD	8.149	−4.642	2.415	8.163	−4.173	2.447
	Hybrid	8.149	−4.404	1.987	8.129	4.392	2.174
0.25	CFD	8.157	−5.627	1.954	8.153	−5.250	1.906
	Hybrid	7.941	−5.308	1.613	8.065	−5.351	1.587
0.30	CFD	8.483	−6.767	1.660	8.488	−6.496	1.691
	Hybrid	8.563	−6.692	1.647	8.65	−6.659	1.533
0.35	CFD	8.677	−7.814	1.244	8.560	−7.481	1.249
	Hybrid	8.981	−8.184	1.401	8.936	−7.809	1.308

2.2.1. Aerodynamics of the Coaxial Rotor

Figure 7 shows the derivative of the normal force of the upper and lower rotors resulting from the hybrid and CFD methods. The derivative of the sectional normal force is

the direct acoustic source term in the F1A equation. This serves as an indicator of impulsive noise. Apart from the self-blade–vortex interactions near 70° and 290° azimuth for the two rotors, fluctuations in aerodynamic load occur at 60° intervals due to the blade-crossover interactions between the upper and lower rotors. The disturbances on the upper rotor are significantly stronger than those on the lower rotor. In addition, the lower rotor has stronger pulse fluctuations on the advance side compared with the retreating side.



(**a**) Upper Rotor, CFD (**b**) Lower Rotor, CFD

(**c**) Upper Rotor, Hybrid (**d**) Lower Rotor, Hybrid

Figure 7. Derivative of the Sectional Normal Force of the Rotor.

Figures 8 and 9 present the sectional normal force and its azimuthal derivative of a coaxial rotor, respectively, at a μ of 0.25 and 0.35. The results obtained by the two methods are compared. A high consistency can be observed in the normal force and derivative trends. Intense load pulses occur at 60° intervals, as shown in Figure 8. The positive pulse values of the two methods are consistent. However, some discrepancy exists for the negative pulses. In addition, the lower rotor experiences load fluctuations induced by the tip vortex of the upper rotor. The hybrid method better captures the disturbances on the advance and retreating sides, while the CFD method has negligible sensitivity on the retreating side. The blade–vortex interaction pulses occurring on the lower rotor at 50° and 320° azimuth are stronger than the blade-crossover pulses, as shown in Figure 9. This indicates that the blade–vortex interactions are likely a prominent noise source for the lower rotor.

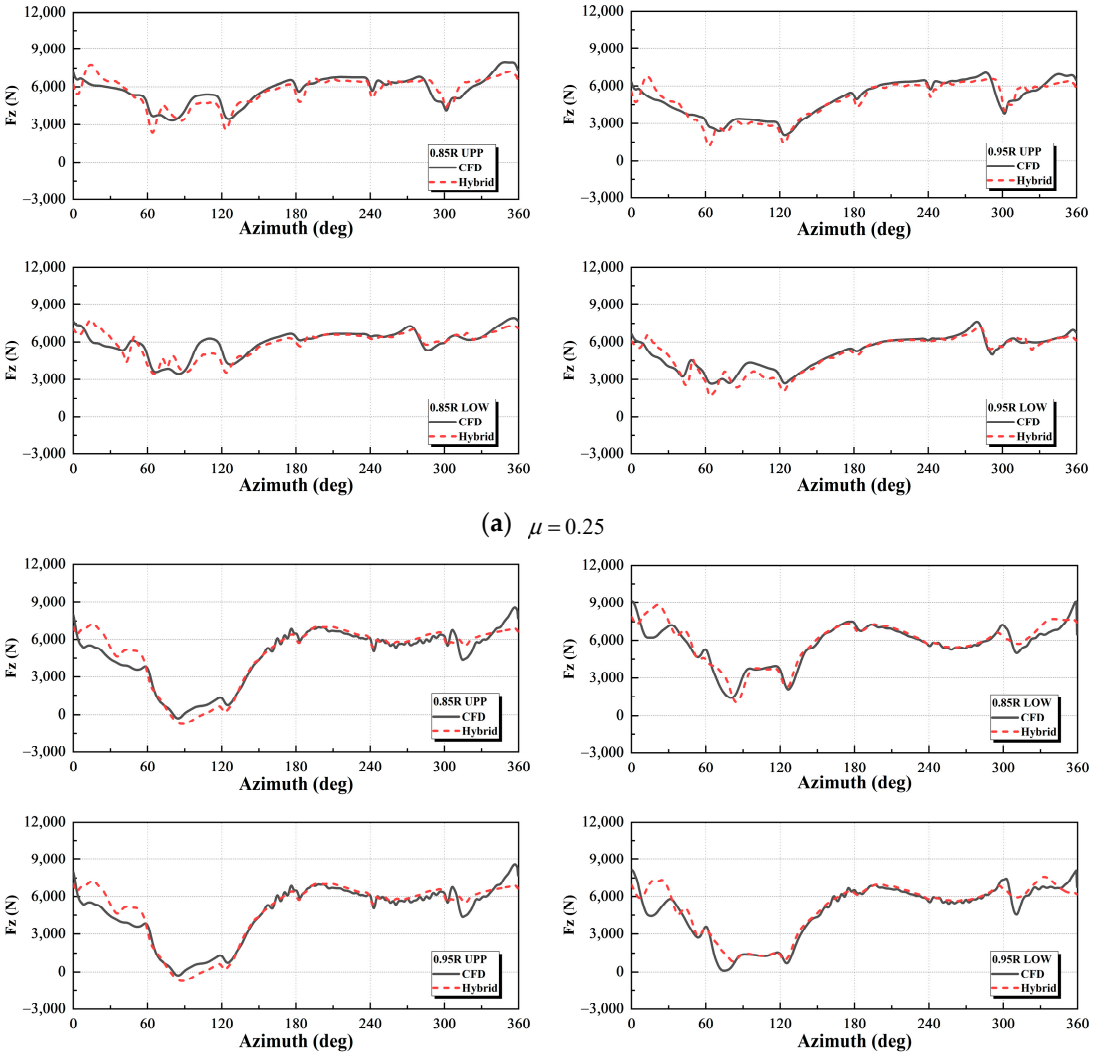


Figure 8. Comparison between the Sectional Normal Forces.

2.2.2. Acoustics of the Coaxial Rotor

Compared with the loading noise, the thickness noise is significantly weaker in the near-field noise composition below the rotor [2]. Thus, a study on the loading noise of the coaxial rotor is conducted. Figure 10 shows the locations of the observation points below the rotor disk, situated on a hemispherical surface with a radius (R) of 28.1075 m (3.5 rotor radii). The upper- and lower-rotor rotation centers coincide with the symmetric center of the hemisphere.

The observation points lie on the symmetric plane of the front bottom region. The coordinates of the observation points are given in Figure 10. Figure 11 shows the acoustic-pressure time histories of the observation points at μ = 0.25. As can be observed in Figure 12, the acoustic-pressure time histories at point #2 are very similar for the two rotors as the observation point is in the symmetric position. There is approximately a 10° phase difference between the loading noise fluctuations of the upper and lower rotors from the difference in distance between the rotors and the observation point. This arises from the difference in propagation distances. The earlier fluctuations are mainly attributed to the lower rotor, which may be due to the more intense blade–vortex interactions. To further validate the consistency between the two approaches, the SPL results from the two models are presented in Figure 13 at μ = 0.25 and 0.35 across all observation points. With the exception of individual outliers, the errors remain below 1.7 dB for the frequency

span analyzed. Given the intrinsically complex nature of the flow-induced noise and the challenges therein for numerical approximation, this level of accuracy is satisfactory and gives confidence in predictions based on this hybrid method.

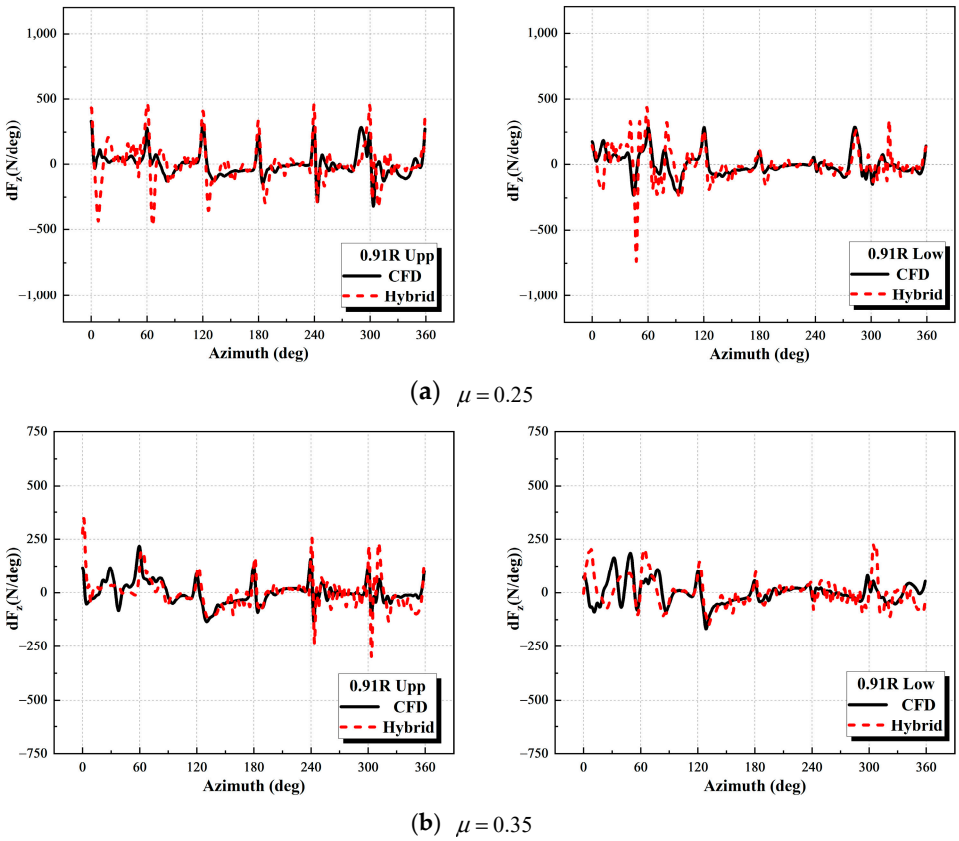
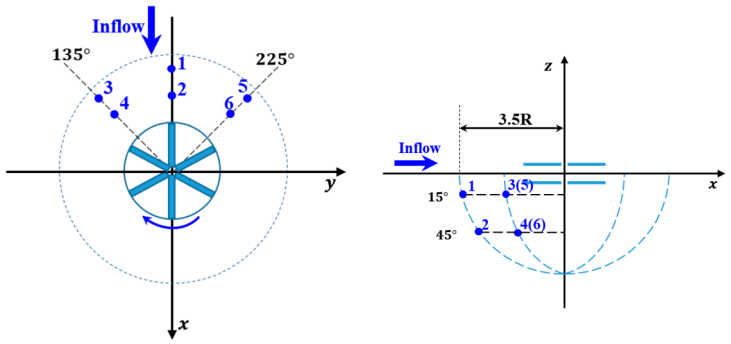


Figure 9. Comparison Between the Azimuthal Derivative of Normal Force.



OBS	Position
#1	(−27.15, 0.0, −7.91)
#2	(−19.88, 0.0, −20.51)
#3	(−19.2, −19.2, −7.91)
#4	(−14.05, −14.05, −20.51)
#5	(−19.2, 19.2, −7.91)
#6	(−14.05, 14.05, −20.51)

Figure 10. Coordinates of the Observers.

It can be seen from Figures 11 and 13 that the prediction results of the coaxial rotor loading noise based on the hybrid method are consistent with those of the CFD method. Although experimental data for the rigid coaxial-rotor model are not available for direct comparison, the agreement between the two different methods partially verifies the validity of the proposed approach.

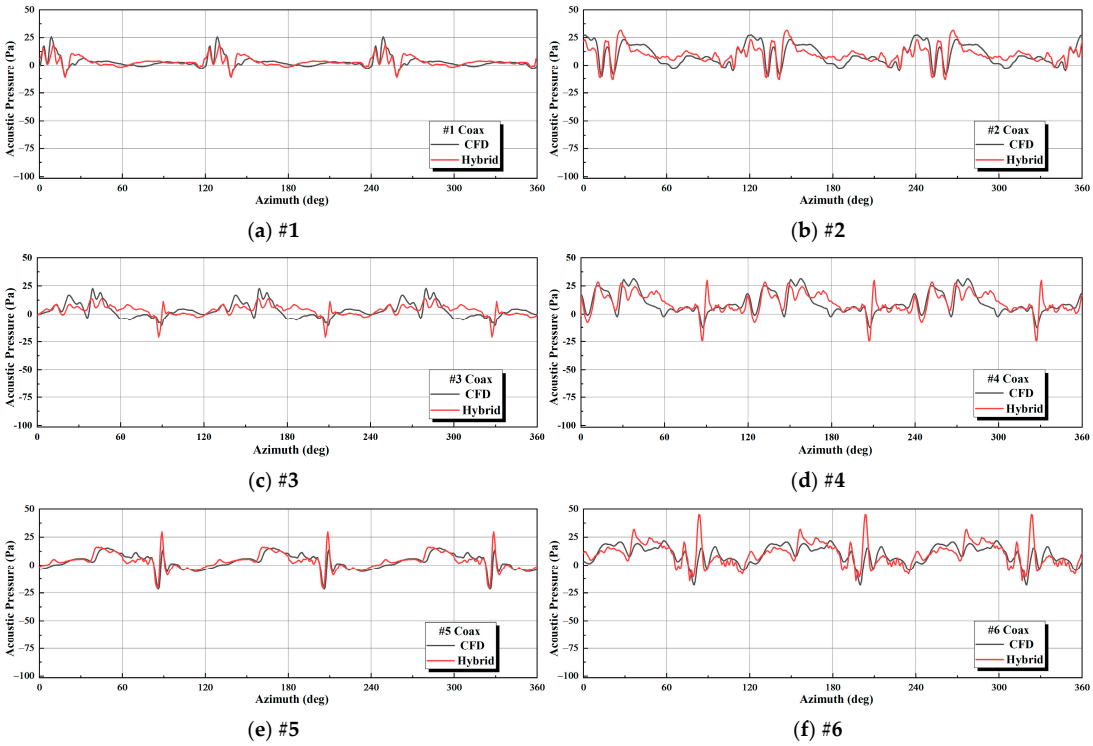


Figure 11. Acoustic-pressure Time History of the Observers.

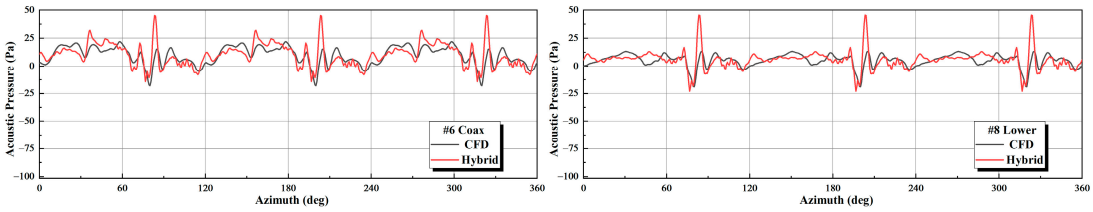


Figure 12. Acoustic-pressure Time History at #2.

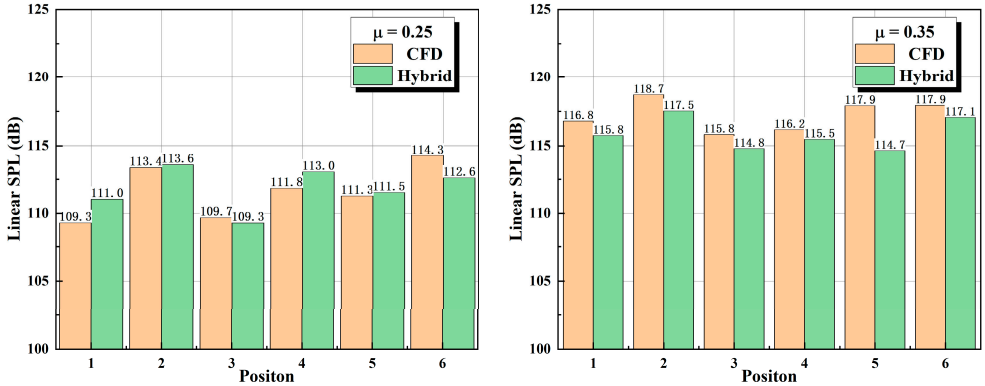
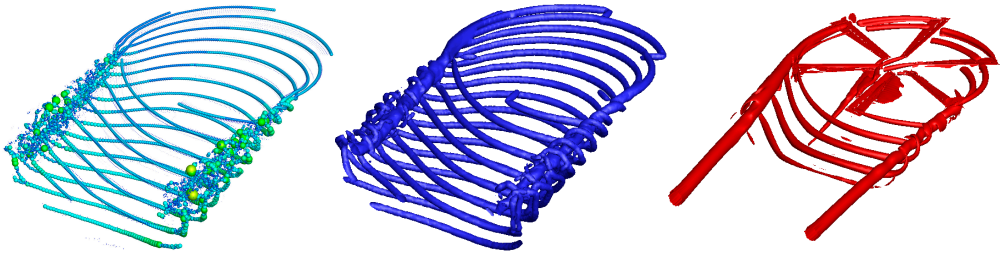


Figure 13. Linear SPL of the Observers.

2.3. Comparison of the Computational Efficiencies

The proposed hybrid method eliminates the computations of the background grid flow field and grids the Chimera interpolation. This allows significant improvement of the computational efficiency, compared with the CFD method. To quantify the efficiency of the hybrid method, single and coaxial rotor cases were analyzed using the same workstation (AMD EPYC 74552 processor at 2.35 GHz). The CFD grids comprise blade grids, fine background grids, and coarse background grids overset with each other, as shown in Figure 2b. For the coaxial rotor, there are 2.01 million volume grid nodes per blade × 3

blades per rotor × 2 rotors, 7.99 million volume grid nodes for the fine background mesh, and 3.12 million volume grid nodes for the coarse background mesh. For the single rotor, there are 1.93 million volume grid nodes per blade × 6 blades, 11.39 million volume grid nodes for the fine background mesh, and 3.12 million volume grid nodes for the coarse background mesh. The fine background grid always guarantees a grid size of 0.1 C (chord length) in its Chimera area and that of the blade grid. The blade mesh used in the hybrid method is similar to that in the CFD method, as illustrated in Figure 2a. The FMM method accelerates the computations of the induced velocity interactions between vortices. The wake calculation time closely correlates with the number of vortices. It is important to mention that the two methods perform parallel grid block computations when calculating the blade grid flow field. Figure 6 presents the wake vortices of the coaxial rotor obtained using the CFD and hybrid methods, while Figure 14 shows the wake vortices for a single rotor obtained by the two approaches. Table 5 presents the computation time of the CFD and hybrid methods. The hybrid method computation procedure mainly consists of three parts: CFD solution of the blade mesh flow field, induced velocity calculations on each facet element of the far-field boundary of the blade grids, and wake convection calculations using the VVPM method. Among these, the CFD module accounts for more than half of the total computation time. It can be seen from Table 5 that in general, the computational efficiency of the hybrid method is improved by a factor of 3–4 compared with the CFD method.



(**a**) Vortex Particle Distribution (**b**) VVPM (**c**) CFD

Figure 14. Wake Vortex of Single Rotor with Vorticity Magnitude of 15.

Table 5. Computational Efficiency of the Methods.

Methods		Single Time Cost	Coaxial Time Cost
Hybrid Method	CFD Block	5.09 h	4.93 h
	VVPM Block	2.48 h	2.57 h
	InducVel Block	1.66 h	1.99 h
	Total	9.23 h	9.49 h
CFD Method		43.06 h	30.3 h
SpeedUp Ratio		4.66	3.19

3. Near-Field Aeroacoustic Characteristics of the Coaxial Rotor

To analyze the near-field noise characteristics of the coaxial rotor, different operating conditions including the advance ratio, tip speed, and incoming flow angle were studied. The coaxial rotor has complex unsteady loading behaviors in forward flight. The impacts of the forward velocity and rotor RPM on the rotor loading noise radiation were studied. To clarify the individual contributions of the upper and lower rotors to the loading noise of the coaxial rotor, the loading noise distributions from each rotor are separately calculated and analyzed. In addition, this study focuses on the maximum loading noise level (peak SPL) in the front half of the observation region, as this metric can more directly and effectively assess the impact on the ground noise.

3.1. Advance Ratio

To investigate the changes in the noise propagation characteristics of the coaxial rotor under different advance ratios, trim adjustments were first performed for each operating

condition, as shown in Table 4. Figure 15 presents the loading noise distributions on the hemispherical observation surface for μ values ranging between 0.15 and 0.30 in 0.05 increments. For μ = 0.20, periodic enhancements in loading noise are observed at 60° azimuthal intervals on the observation surface. This phenomenon also appears in the upper-rotor acoustic-pressure level distribution, which is attributed to more intense pulsating loads caused by blade-crossover interactions. By examining the noise distributions across the advance ratio, it can be deduced that the noise hotspots are consistently located slightly below and forward of the rotor disk. It can be observed from Figure 16 that, in addition to the primary acoustic-pressure pulse resulting from the in-phase superposition of the upper- and lower-rotor loading noises, the secondary pulses also largely maintain the same inter-rotor phasing.

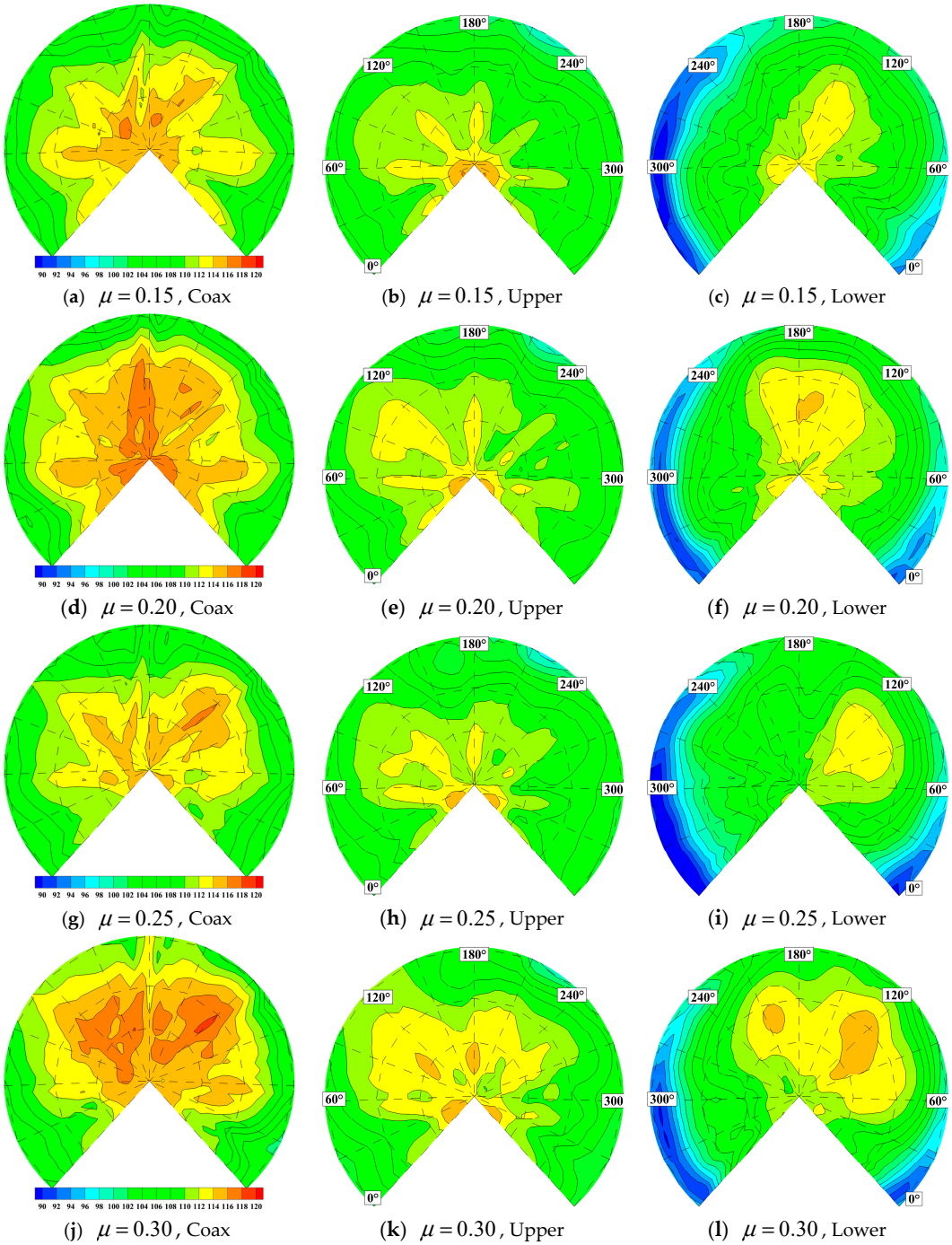


Figure 15. SPL on the Observation Plane at Different Advance Ratios.

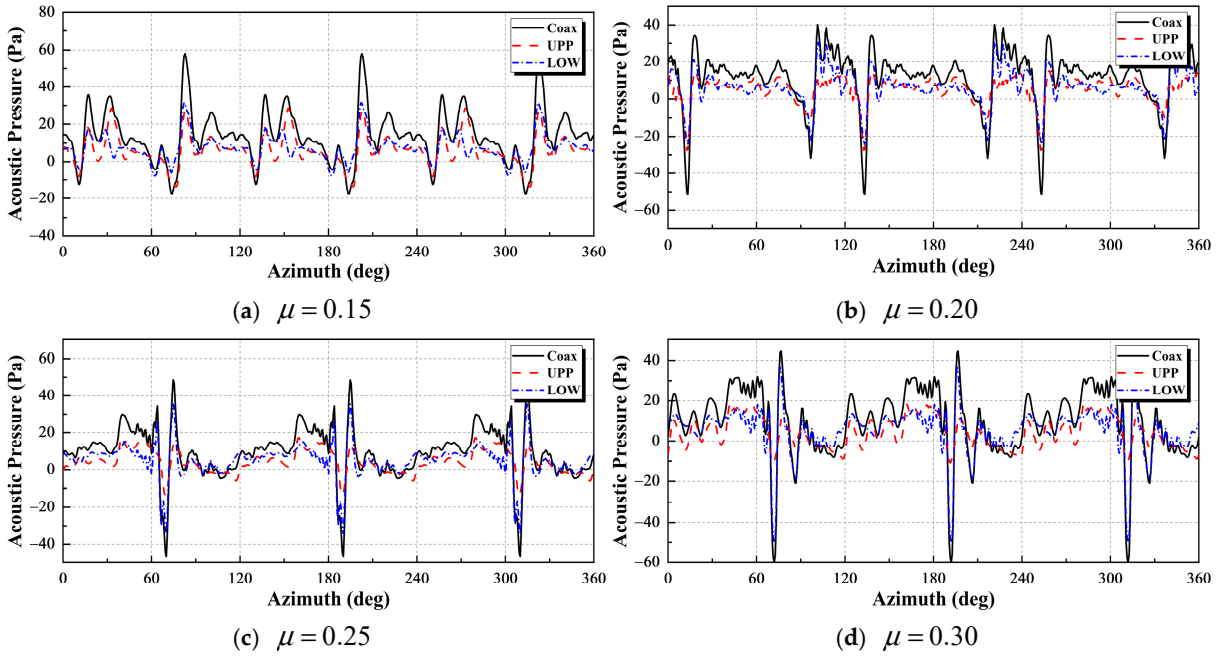
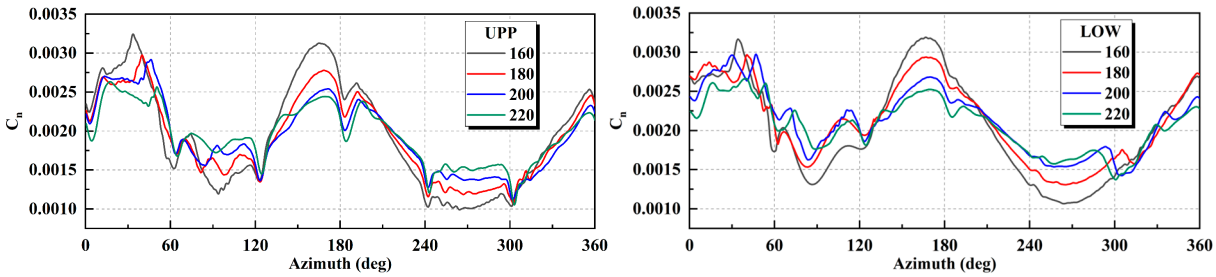


Figure 16. Acoustic pressure of Peak SPL at Different Advance Ratios.

3.2. Tip Velocity

At low flight velocities, the coaxial rotor operates at relatively high RPM to generate requisite lift. When the flight speed increases, the rotor RPM is reduced to prevent exceeding the critical tip Mach number on the advancing side and resultant shockwave generation. This induces changes in the noise characteristics of the coaxial rotor.

Therefore, computations are performed on a rigid coaxial rotor at μ = 0.30, which corresponds to a V_{tip} of 220 m/s. The advancing side tip Mach numbers vary from 0.567 to 0.840. The trim results are shown in Table 6. Figure 17 shows the instantaneous blade loads at different tip speed, which highlights the variation in the blade lift coefficient at a fixed advance ratio for various tip speeds. The load impulses arising from blade interactions become more perceptible at a higher tip speed. Similarly, the acoustic-pressure level distribution of the upper-rotor loading noise has increasing periodicity with the increase in the tip speed, as shown in Figure 18. The lower-rotor loading noise distribution remains largely invariant, with hotspots situated on the advancing side. The peak SPL of the coaxial, upper, and lower rotors intensify with the increase in the tip speed, as shown in Figure 19. The superimposition of the load noise from the upper and lower rotors results in the peak SPL of the coaxial rotor being much higher compared to that of either the upper rotor or the lower rotor.

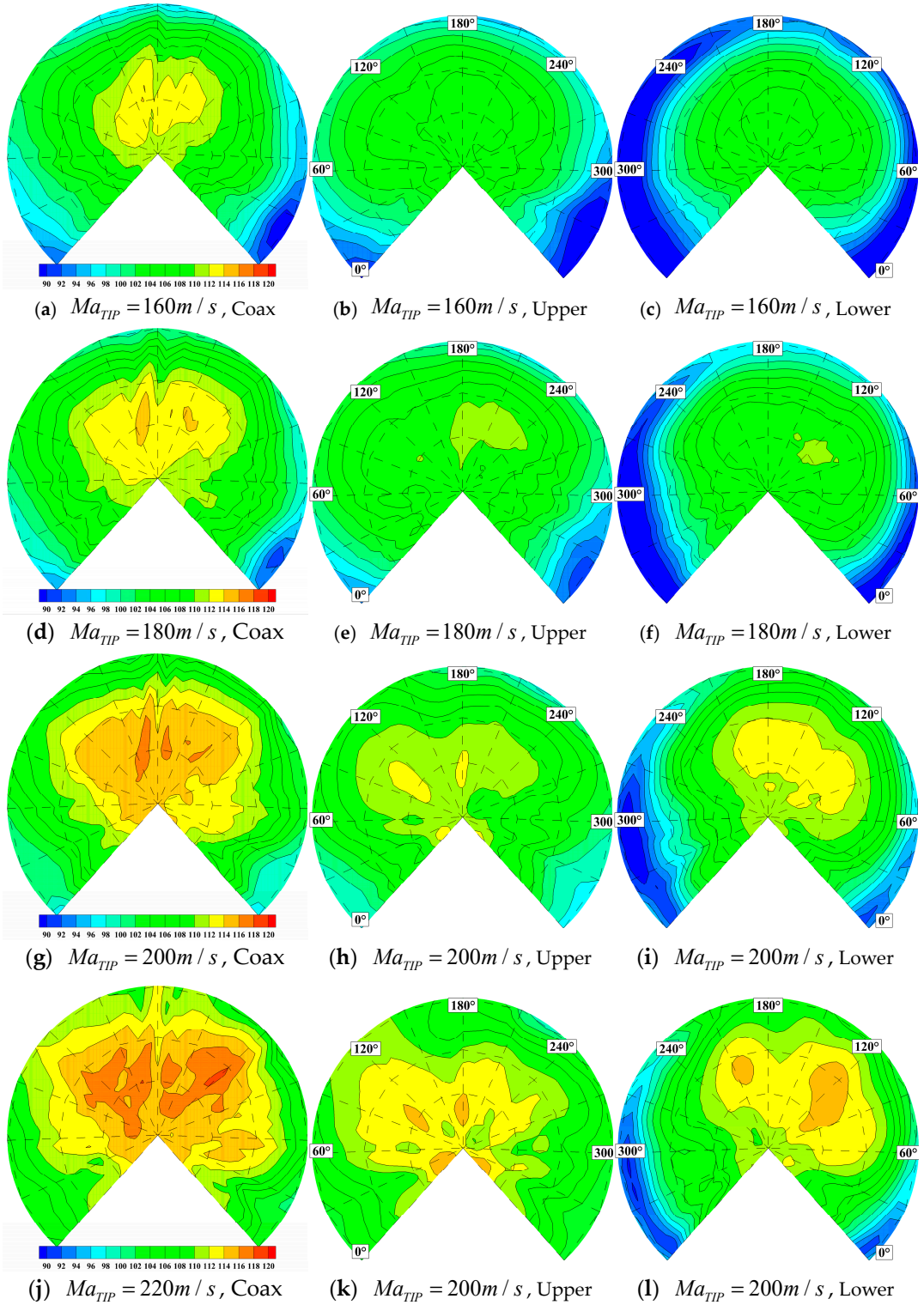


Lift Coefficients of Upper Rotor Lift Coefficients of Upper Rotor

Figure 17. Instantaneous Blade Loads at Different Tip Speeds.

Table 6. Pitch control for different tip speeds.

Ma_{tip}	Ma_{AT}	$\theta_{0upp}/(°)$	$\theta_{1supp}/(°)$	$\theta_{1cupp}/(°)$	$\theta_{0low}/(°)$	$\theta_{1slow}/(°)$	$\theta_{1clow}/(°)$
0.470	0.664	8.563	−6.692	1.647	8.655	−6.659	1.601
0.529	0.723	9.666	−7.890	2.424	9.643	−7.712	2.256
0.579	0.782	9.850	−8.765	1.908	9.814	−8.417	1.682
0.647	0.840	10.180	−9.726	1.351	10.180	−9.545	1.141



(**a**) $Ma_{TIP} = 160m/s$, Coax (**b**) $Ma_{TIP} = 160m/s$, Upper (**c**) $Ma_{TIP} = 160m/s$, Lower

(**d**) $Ma_{TIP} = 180m/s$, Coax (**e**) $Ma_{TIP} = 180m/s$, Upper (**f**) $Ma_{TIP} = 180m/s$, Lower

(**g**) $Ma_{TIP} = 200m/s$, Coax (**h**) $Ma_{TIP} = 200m/s$, Upper (**i**) $Ma_{TIP} = 200m/s$, Lower

(**j**) $Ma_{TIP} = 220m/s$, Coax (**k**) $Ma_{TIP} = 200m/s$, Upper (**l**) $Ma_{TIP} = 200m/s$, Lower

Figure 18. SPL on the Observation Plane at Different Blade Tip Speeds.

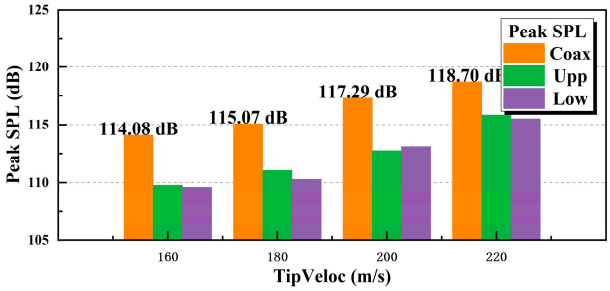
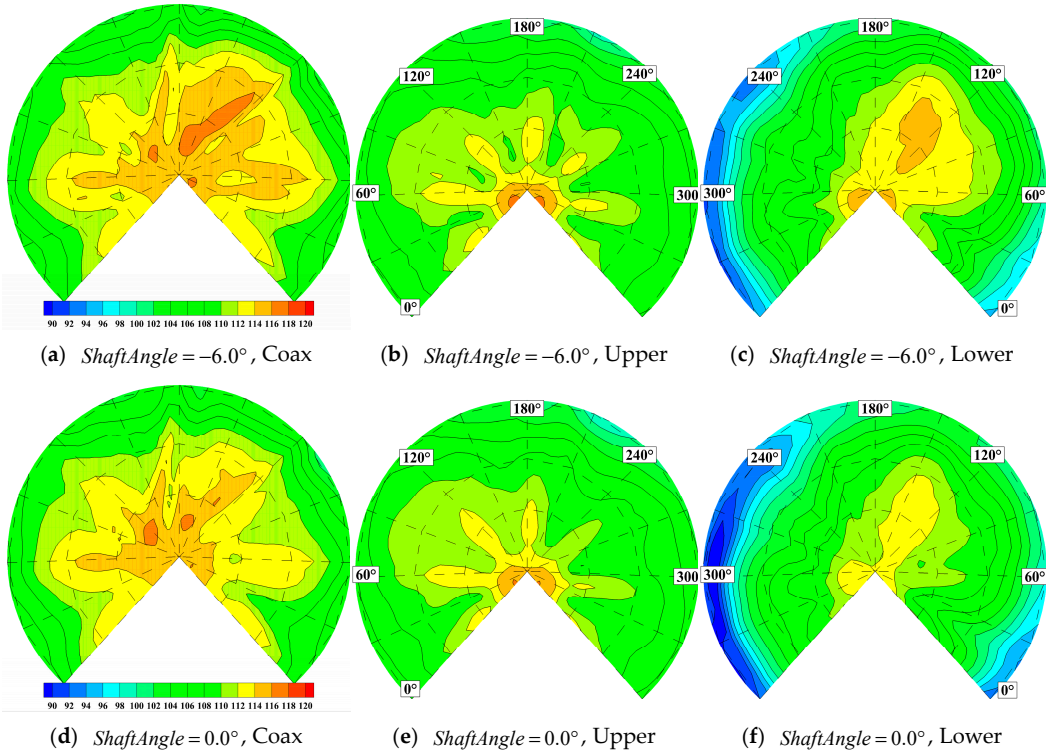


Figure 19. Peak SPL at Different Blade Tip Speeds.

3.3. Shaft Angle

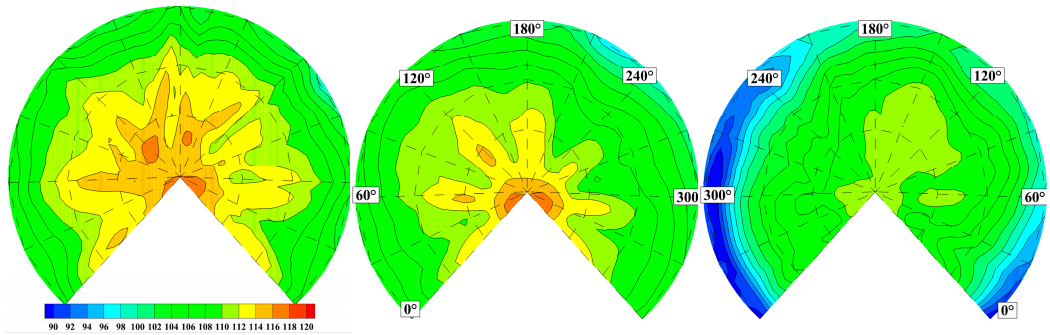
Figures 20 and 21 shows the SPL distributions on the observation plane at different shaft angle for the coaxial rotor at μ = 0.15 and μ = 0.3. It can be seen from Figure 20 that notable periodic enhancements in the acoustic-pressure level are still exhibited by the upper rotor at various shaft angles under the low advance ratio. However, it can be observed from Figure 21 that at a high advance ratio, the periodicity of the upper-rotor loading noise is less pronounced, and it remains more affected by the blade-crossover interferences compared with the lower rotor. Moreover, it can be deduced that the loading noise distribution of the upper rotor is relatively invariant with the changes in the shaft angle, while the lower-rotor loading noise distribution is significantly affected, especially when it substantially increases. Figure 22 illustrates the instantaneous lift at different advance ratios. At the low forward ratio, the trends of lift changes are relatively consistent across different shaft angles. However, at the high advance ratio, the thrust trends demonstrate more significant differences. Theoretically, the aerodynamic interaction between the upper and lower rotor is more pronounced at the smaller advance ratio. Nevertheless, as the velocity of the forward flight increases, the tip vortex intensity of the rotor also intensifies. Therefore, at the high advance ratio, the effects of aerodynamic interaction and related instantaneous load variations caused by tip vortex at different shaft angles are greater compared to the low advance ratio condition.



(**a**) *ShaftAngle* = −6.0°, Coax (**b**) *ShaftAngle* = −6.0°, Upper (**c**) *ShaftAngle* = −6.0°, Lower

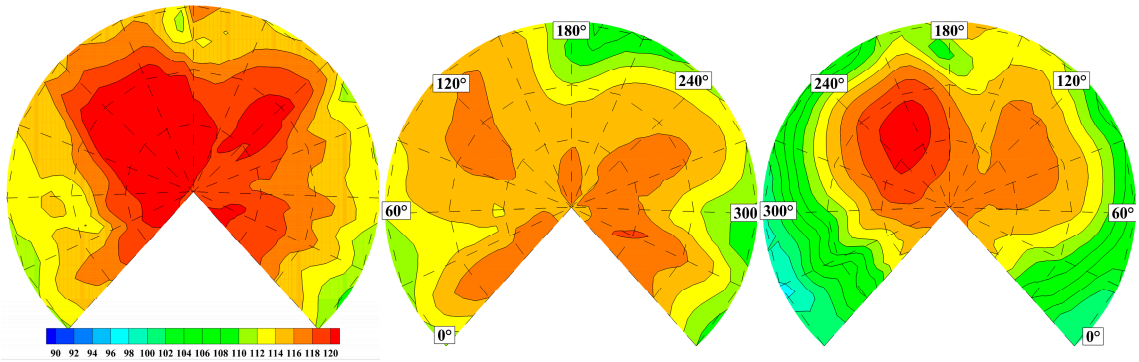
(**d**) *ShaftAngle* = 0.0°, Coax (**e**) *ShaftAngle* = 0.0°, Upper (**f**) *ShaftAngle* = 0.0°, Lower

Figure 20. *Cont.*

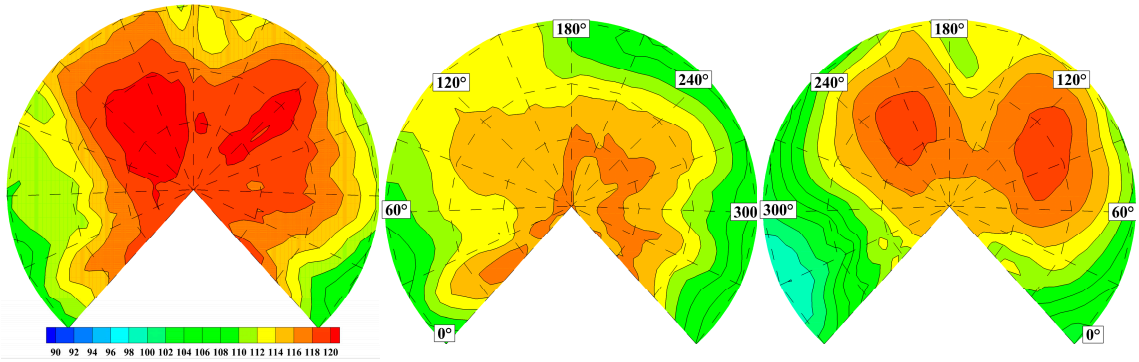


(**g**) *ShaftAngle* = 6.0°, Coax (**h**) *ShaftAngle* = 6.0°, Upper (**i**) *ShaftAngle* = 6.0°, Lower

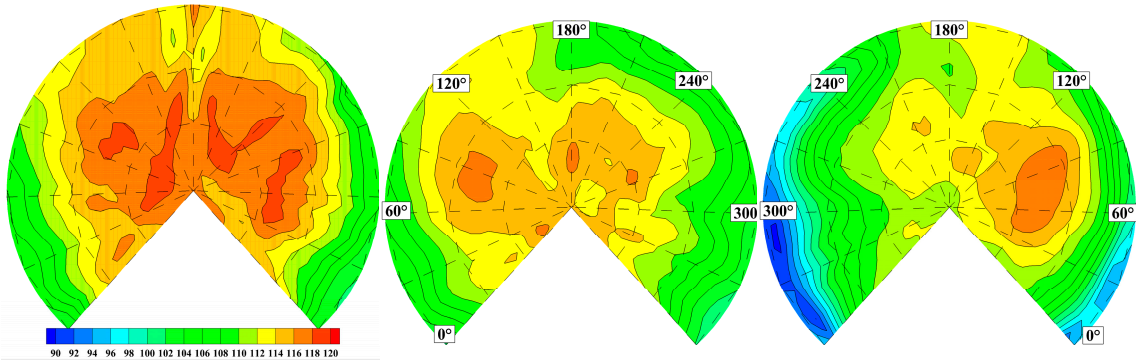
Figure 20. SPL on the observation plane at $\mu = 0.15$.



(**a**) *ShaftAngle* = −6.0°, Coax (**b**) *ShaftAngle* = −6.0°, Upper (**c**) *ShaftAngle* = −6.0°, Lower

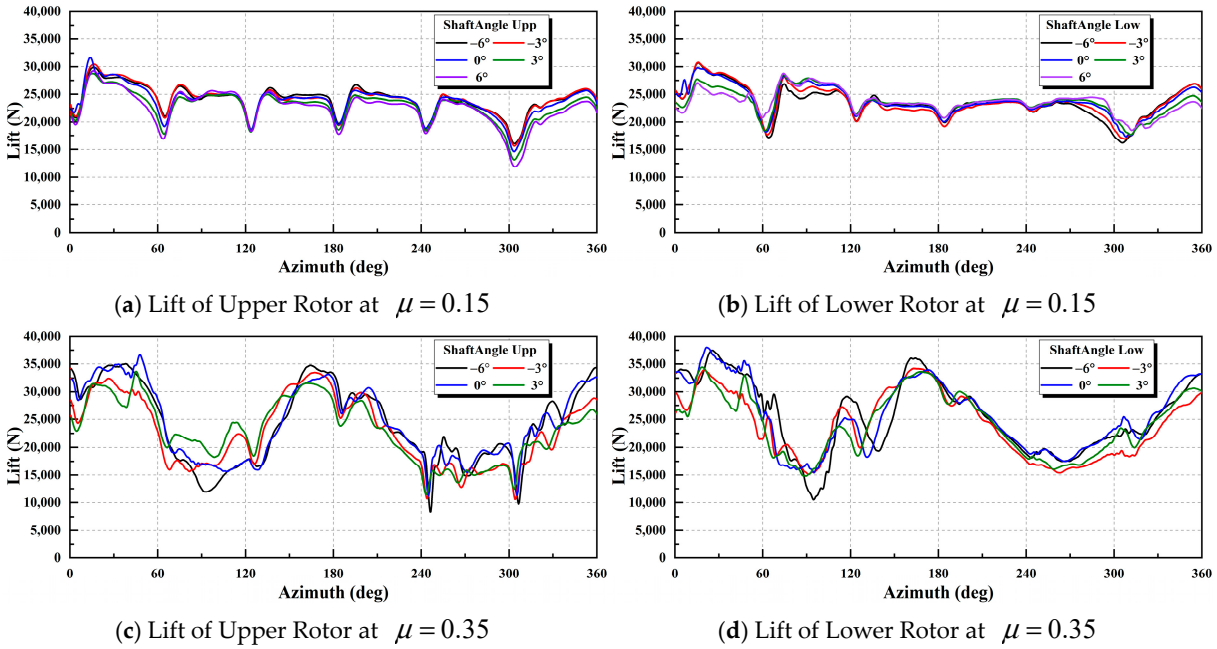


(**d**) *ShaftAngle* = 0.0°, Coax (**e**) *ShaftAngle* = 0.0°, Upper (**f**) *ShaftAngle* = 0.0°, Lower



(**g**) *ShaftAngle* = 3.0°, Coax (**h**) *ShaftAngle* = 3.0°, Upper (**i**) *ShaftAngle* = 3.0°, Lower

Figure 21. SPL on the observation plane at $\mu = 0.35$.

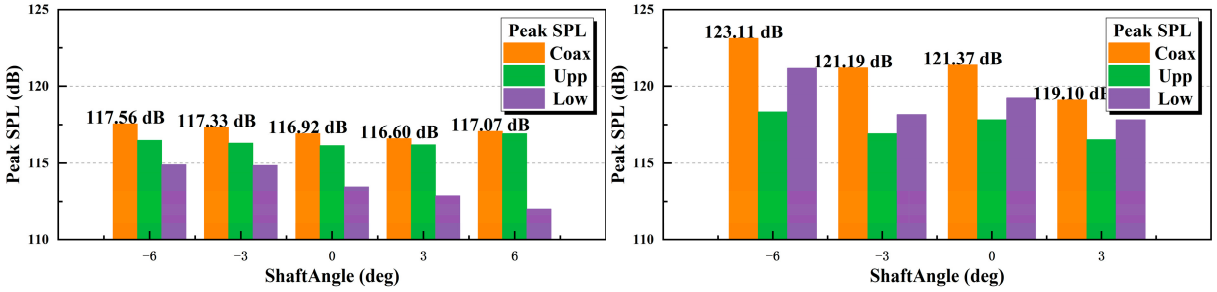


(**a**) Lift of Upper Rotor at $\mu = 0.15$ (**b**) Lift of Lower Rotor at $\mu = 0.15$

(**c**) Lift of Upper Rotor at $\mu = 0.35$ (**d**) Lift of Lower Rotor at $\mu = 0.35$

Figure 22. Instantaneous Blade Forces at Different Shaft Angles.

Especially in the case of $-6°$, the SPL distribution is significantly higher than that in other states, and the max SPL in Figure 23 also shows the same trend. Although the backward shaft angle will generally cause a more serious self-blade–vortex interaction, the wake of the upper rotor will develop faster and will be downward in the case of the forward shaft angle. This results in an increase in the interaction intensity between the wake of the upper rotor and the blade of the lower rotor The intensity of the loading noise in the case in the forward state is larger than that in the backward state. This result reflects that the contribution of the inter-rotor-blade–vortex interaction to loading noise is greater than that of the self-blade–vortex interaction.



(**a**) $\mu = 0.15$ (**b**) $\mu = 0.35$

Figure 23. Peak SPL on the Observation Plane at Different Shaft Angles.

At a low advance ratio, the upper rotor has higher SPL distributions at all shaft angles compared with the lower rotor, and the peak SPL is higher for the upper rotor. Hence, the loading noise of the upper-rotor contribution prevails, and that of the coaxial-rotor distribution resembles that of the upper rotor. This is due to the fact that at a low advance ratio, the blade-crossover load fluctuation intensity exceeds the blade–vortex interaction load fluctuation. The reverse happens at a high advance ratio, where the peak SPL of the lower rotor surpasses that of the upper rotor. This indicates that the blade–vortex interaction load fluctuation is dominant over the blade-crossover load fluctuation.

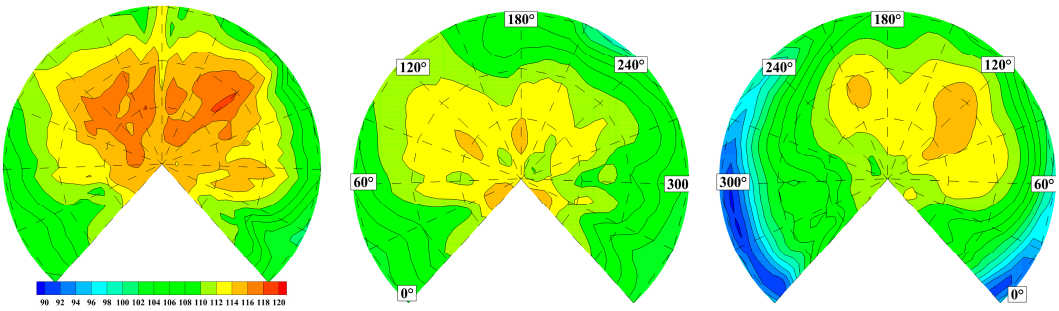
4. Analysis of the Effects of the Parameters

The blade–vortex interaction between the wake of the upper rotor and the blades of the lower rotor is an additional noise source that does not exist in the flow field of the single rotor, making an important contribution to the noise of coaxial rotors. Therefore, by adjusting the vertical spacing between the upper and lower rotors and the initial phase of the rotors, this interaction can be altered to mitigate the blade–vortex interaction noise. Calculations are then performed with adjustments to the vertical spacing and initial phase between the upper and lower rotors, in order to evaluate the sensitivity of the radiated noise of the coaxial rotor to such design changes.

4.1. Initial Phase

In contrast to single rotors, modulating the initial phase angle between the upper and lower rotors directly alters the inter-rotor blade interactions, which induces variations in the vortex flow around the rotors. Thus, this significantly affects the near-field noise generation. The near-field acoustic performance of the coaxial rotor can be effectively enhanced by optimizing the inter-rotor initial phase. Hence, calculations are performed on different initial phase combinations of the two rotors to determine the phase match yielding minimal near-field noise.

Taking $\mu = 0.3$ and $V_{tip} = 220$ m/s as the baseline, four distinct upper-rotor initial azimuth angles of $\psi_0 = [0°, 30°, 60°, 90°]$ were specified while maintaining a constant lower rotor, with $\psi_0 = 0°$ denoting the initial azimuth. Figure 24 reveals the distribution of loading noise under different initial azimuth angles. it is observed that the loading noise distribution of the upper rotor is not obvious, while the hotspot of loading noise of the lower rotor is significant and its position remains stable. Especially at the initial azimuth angle of 30°, the SPL in the vicinity of this hotspot is significantly higher than other states. The implemented pitch controls are presented in Table 4. It can be seen from Figure 25 that the variations in the loading noise hotspots of the upper rotor are constrained within 1 dB under diverse start-up angle conditions. Meanwhile the lower and coaxial rotors show consistent loading noise variation trends with greater fluctuations. It can be deduced from the instantaneous blade forces in Figure 26 that intense blade-vortex-interaction load fluctuations arise around the 50° azimuth for the 30° initial phase angle condition compared with other start-up cases. Correspondingly, the coaxial rotor achieves the maximum peak SPL of 119.98 dB for this condition. On the contrary, the 90° start-up angle has small blade–vortex-interaction load fluctuations in the instantaneous blade forces of Figure 25, and corresponds to the peak SPL of 116.7 dB. The difference in the peak SPL on the front hemisphere observation plane surpasses 3 dB for the coaxial rotor under different start-up angles. It can be observed that even a relatively crude phase matching can significantly affect the aerodynamic interactions between the rotors, which modifies the near-field noise and optimizes the acoustic performance.



(**a**) *InitialPhase* = 0.0° , Coax (**b**) *InitialPhase* = 0.0° , Upper (**c**) *InitialPhase* = 0.0° , Lower

Figure 24. *Cont.*

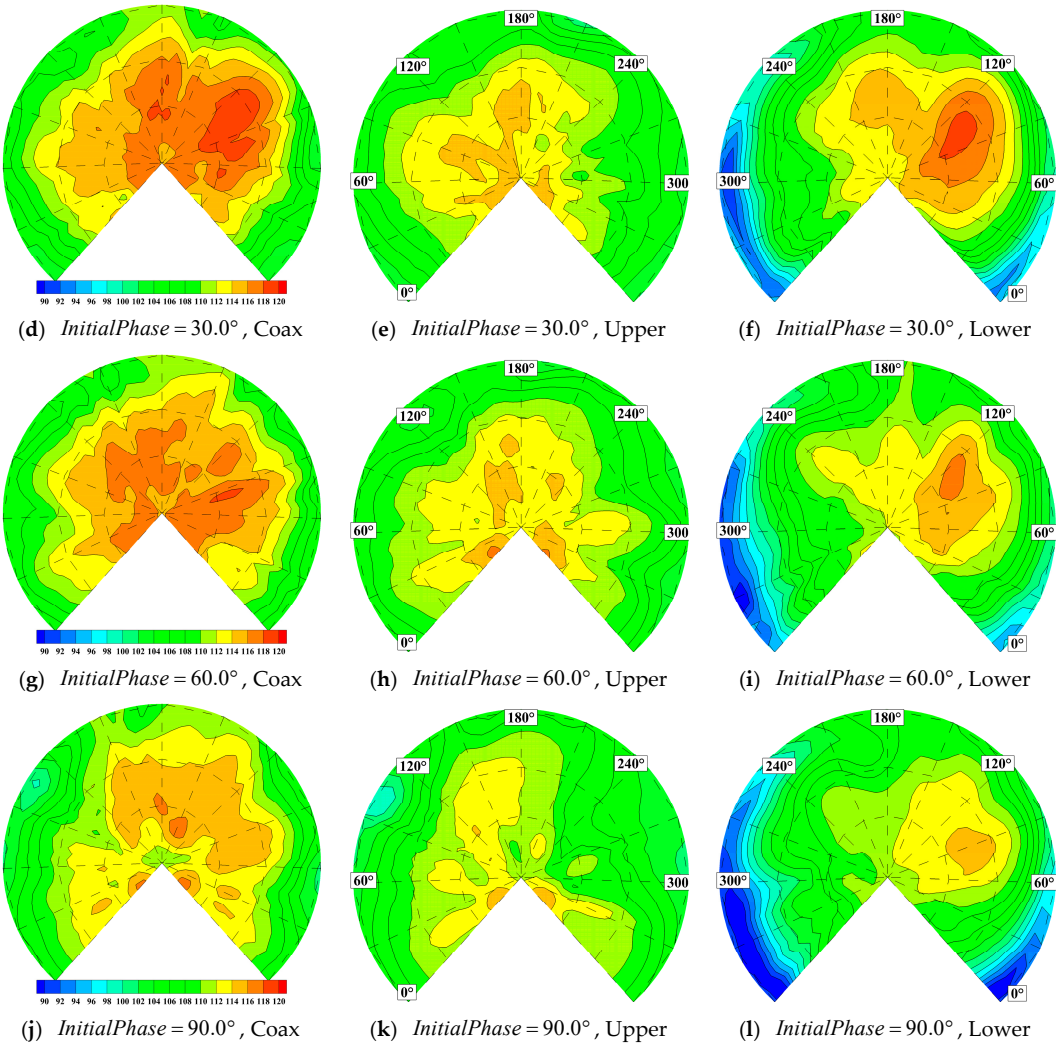


Figure 24. SPL on Observation Planes at Different Initial Azimuth values.

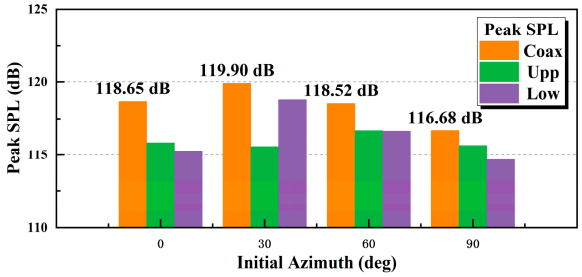
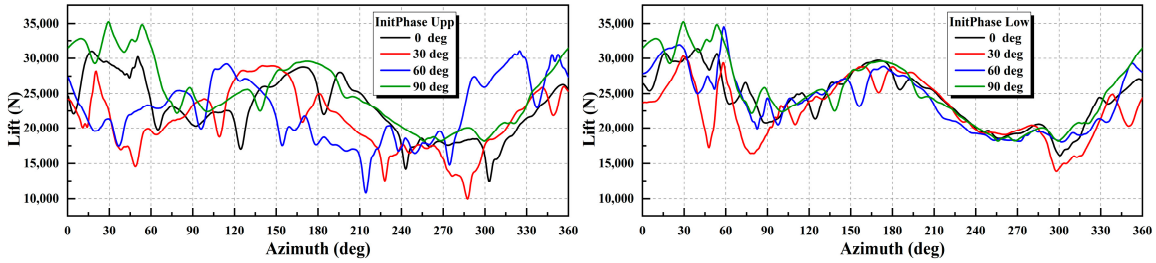


Figure 25. Peak SPL at Different Initial Azimuth values.

4.2. Vertical Spacing

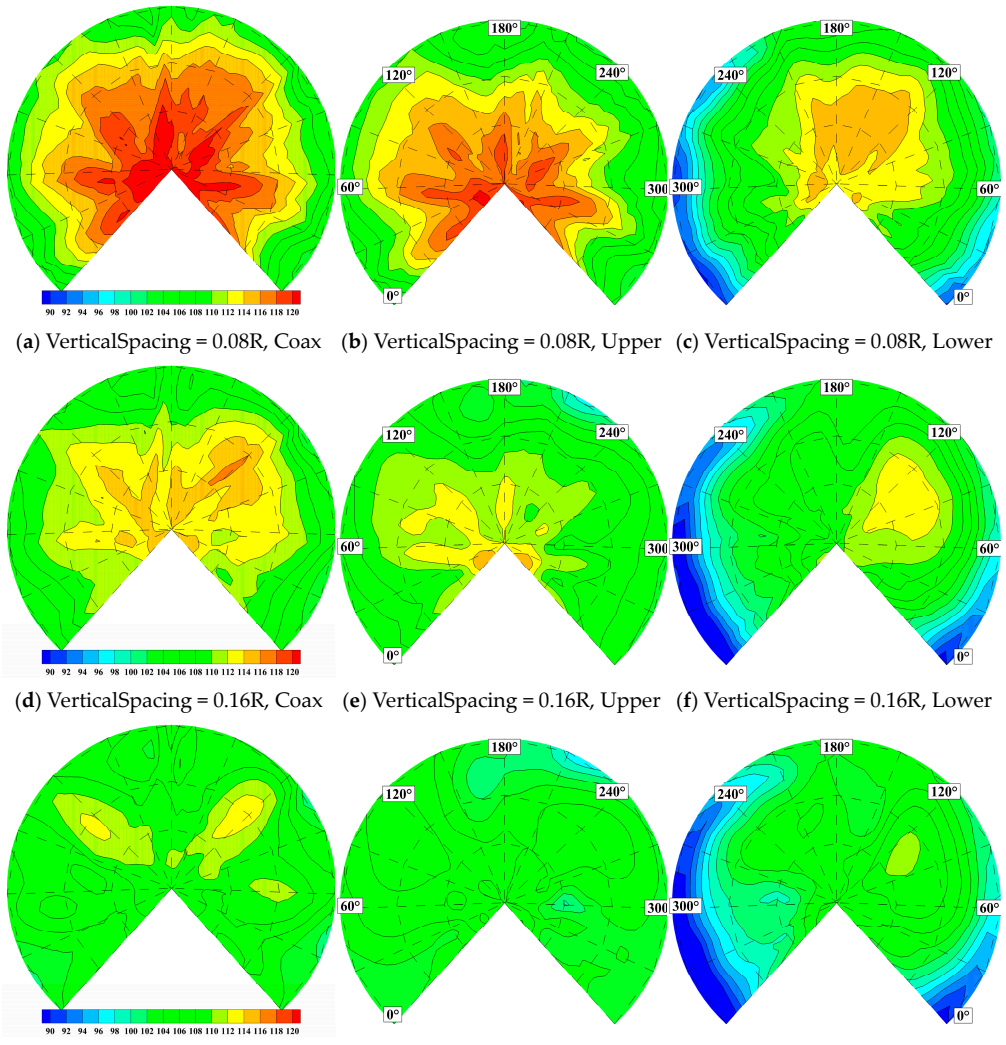
Figure 27 presents the distributions of rotor loading noise for inter-rotor vertical spacing ranging between 0.08 R and 0.24 R at μ = 0.15. It can be clearly observed that at small vertical spacing, the distributions of loading noise of the coaxial and upper rotors have strong periodicity. This indicates severe blade-crossover-load interference between the upper and lower rotors, as shown in Figure 28. In the minimum vertical spacing condition, the load fluctuation intensity of the upper rotor is significantly higher at every 60° azimuth, compared with the other spacing cases. When the spacing increases, the loading noise characteristics of the upper and lower rotors become almost symmetrically distributed along the incoming velocity direction, and the instantaneous blade forces of the upper rotor

no longer exhibit significant load pulsations, as shown in Figure 29. When the vertical spacing increases from 0.08 R to 0.24 R, the peak SPL on the observation plane gradually decreases for the coaxial, upper, and lower rotors. The peak SPL of the coaxial rotor decreases by almost 10.1 dB, while those of the upper and lower rotors decrease by 12.6 dB and 5.2 dB, respectively. It can be observed that the reduction rate of the peak SPL for the upper rotor is significantly higher than that of the lower rotor. At a vertical spacing of 0.24 R, the peak SPL of the lower rotor exceeds that of the upper rotor. Therefore, appropriately adjusting the rotor spacing can effectively modify the loading noise characteristics and perform noise reduction for the coaxial rotor.



(**a**) Lift of Upper Rotor (**b**) Lift of Lower Rotor

Figure 26. Instantaneous Blade Forces at Different Initial Azimuth values.

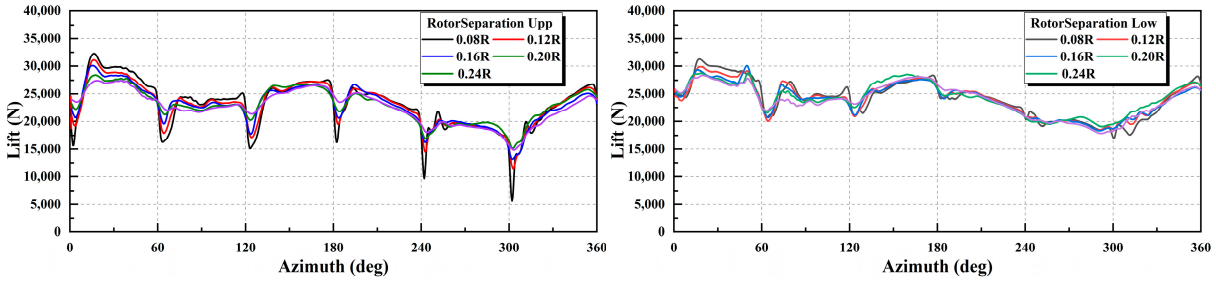


(**a**) VerticalSpacing = 0.08R, Coax (**b**) VerticalSpacing = 0.08R, Upper (**c**) VerticalSpacing = 0.08R, Lower

(**d**) VerticalSpacing = 0.16R, Coax (**e**) VerticalSpacing = 0.16R, Upper (**f**) VerticalSpacing = 0.16R, Lower

(**g**) VerticalSpacing = 0.24R, Coax (**h**) VerticalSpacing = 0.24R, Upper (**i**) VerticalSpacing = 0.24R, Lower

Figure 27. SPL on Observation Planes at Different Vertical Spacings.



(**a**) Lift of Upper Rotor (**b**) Lift of Lower Rotor

Figure 28. Instantaneous Blade Forces at Different Vertical Spacings.

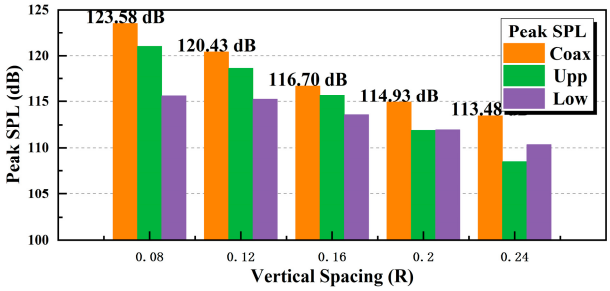


Figure 29. Peak SPL at Different Vertical Spacings.

5. Conclusions

In this study, a CFD/VVPM method for coaxial-rotor acoustic prediction and analysis was proposed. The aerodynamic and acoustic characteristics of the coaxial rotor were simulated and compared based on the hybrid method and CFD method. In addition, methods to alter the load noise propagation characteristics of the coaxial rotor for reducing the near-field noise were explored. The conclusions are summarized as follows:

Compared with the CFD method based on the Chimera interpolation method, the proposed CFD/VVPM hybrid method improves the computational efficiency by three to four orders of magnitude. This method has significant advantages in capturing the aerodynamic characteristics of the blade–vortex interaction, and it can accurately simulate the noise characteristics of a rigid coaxial rotor.

The upper rotor is mainly affected by the blade-crossover interaction, which results in periodic enhancements in the loading noise pressure levels on the observer plane, which becomes more pronounced at smaller advance ratios. On the contrary, the lower rotor is mainly affected by the blade–vortex interactions, and the loading noise distribution is analogous to that of a single rotor. The peak SPL of the upper rotor exceeds that of the lower rotor on the observer plane at small advance ratios. However, when the advance ratio increases, the lower-rotor peak SPL gradually surpasses that of the upper rotor

At a low blade tip speed, the direct interactions between the upper and lower rotors is weaker. This yields similar loading noise distributions between the two rotors. When the blade tip speed increases, the periodic loading noise distribution of the upper rotor becomes more pronounced on the observer plane.

The shaft angle leads to intensified rotor–wake interactions, having a greater impact on the SPL distribution of the lower rotor and increasing the overall SPL of the coaxial rotors. The peak SPL of the upper rotor is higher than that of the lower rotor at low advance ratios. However, when the advance ratio increases, the peak SPL of the lower rotor exceeds that of the upper rotor.

The coaxial rotors have high blade–vortex interaction noise. However, the loading noise can be mitigated through passive rotor design by adjusting the initial phase and rotor spacing. The obtained results demonstrate that shifting the upper-rotor initial phase to 30° alleviates the rotor–wake interactions between the upper and lower rotors. This reduces the

peak SPL by greater than 3 dB under the same flight conditions. In addition, significantly increasing the rotor spacing weakens the aerodynamic interference, and when the spacing increases from 0.08 R to 0.24 R, the peak SPL decreases by more than 10 dB.

It is anticipated that this approach will be applied in future research to predict noise throughout the full flight envelope of coaxial rotors. This will enable simulations of the impact of dynamic changes on noise under various flight conditions, such as takeoff, climb, level flight, turn, and descent for landing. This approach can also be integrated into the simulation prediction of active noise control techniques, facilitating the design of controller parameters and the assessment of control effectiveness. However, the 'reformulated VPM' method will be coupled in the hybrid method. This enhances the local conservation of mass and angular momentum, to improve numerical stability during the vortex deformation process.

Author Contributions: Conceptualization, G.X. and Y.S.; Methodology, Y.Y.; Software, Y.Y. and Z.H.; Validation, Y.Y. and Z.H.; Formal Analysis, Y.Y.; Investigation, Y.Y.; Resources, Y.Y. and Z.H.; Data Curation, Y.Y.; Writing—original draft preparation, Y.Y.; Writing—review and editing, G.X. and Y.Y.; Visualization, Y.Y. All authors have read and agreed to the published version of the manuscript.

Funding: This research was funded by the National Key Laboratory Foundation of China (ID: 6142202202), the National Natural Science Foundation of China (Grant Number: 11972190), the National Natural Science Foundation of China (Grant Number: 12032012).

Data Availability Statement: The data used to support the findings of this study are available from the corresponding author upon request.

Conflicts of Interest: The authors declare no conflict of interest.

References

1. Jia, Z.; Lee, S. Impulsive Loading Noise of a Lift-Offset Coaxial Rotor in High-Speed Forward Flight. *AIAA J.* **2020**, *58*, 687–701. [CrossRef]
2. Jia, Z.; Lee, S. Aeroacoustic Analysis of a Lift-Offset Coaxial Rotor Using High-Fidelity CFD/CSD Loose Coupling Simulation. *J. Am. Helicopter Soc.* **2020**, *65*, 1–15. [CrossRef]
3. Jia, Z.; Lee, S. Aerodynamically induced noise of a lift-offset coaxial rotor with pitch attitude in high-speed forward flight. *J. Sound Vib.* **2020**, *491*, 115737. [CrossRef]
4. Zhu, Z.; Zhao, Q. Analyses on Aeroacoustic Characteristics of Coaxial Rotor in Forward Flight. In Proceedings of the 74th American Helicopter Society Annual Forum, Phoenix, AZ, USA, 14–17 May 2018.
5. Wang, B.; Cao, C.; Zhao, Q.; Yuan, X.; Zhu, Z. Aeroacoustic Characteristic Analyses of Coaxial Rotors in Hover and Forward Flight. *Int. J. Aeronaut. Space Sci.* **2021**, *22*, 1278–1292. [CrossRef]
6. Singh, P. Aeromechanics of Coaxial Rotor Helicopters using the Viscous Vortex Particle Method. Doctoral Dissertation, University of Michigan, Ann Arbor, MI, USA, 2020.
7. Brentner, K.S. Prediction of helicopter rotor discrete frequency noise for three scale models. *J. Aircr.* **1988**, *25*, 420–427. [CrossRef]
8. Sharma, K.; Brentner, K.S.; Jia, Z.; Lee, S. Aeroacoustic study of lift offset coaxial rotor using free wake analysis. In Proceedings of the Vertical Flight Society's 75th Annual Forum and Technology Display, Philadelphia, PA, USA, 13–16 May 2019.
9. Brown, R.E. Rotor wake modeling for flight dynamic simulation of helicopters. *AIAA J.* **2000**, *38*, 57–63. [CrossRef]
10. Brown, R.E.; Line, A.J. Efficient high-resolution wake modeling using the vorticity transport equation. *AIAA J.* **2005**, *43*, 1434–1443. [CrossRef]
11. Kim, H.W.; Duraisamy, K.; Brown, R. Effect of rotor stiffness and lift offset on the aeroacoustics of a coaxial rotor in level flight. In Proceedings of the 65th American Helicopter Society Annual Forum, Texas, TX, USA, 7–29 May 2009.
12. Kim, H.W.; Duraisamy, K.; Brown, R. Aeroacoustics of a coaxial rotor in level flight. In Proceedings of the 64th American Helicopter Society Annual Forum, Montreal, QU, Canada, 28 April–1 May 2008.
13. Egolf, T.A.; Rajmohan, N.; Reed, E.; Sankar, L.N. A hybrid CFD method for coaxial rotor performance prediction in forward flight. In Proceedings of the AHS Specialist's Conference on Aeromechanics, San Francisco, CA, USA, 20–22 January 2010.
14. Zhao, J.; He, C.; Zhang, L.; Zhao, H.; Hu, P. Coupled viscous vortex particle method and unstructured computational fluid dynamics solver for rotorcraft aerodynamic interaction analysis. In Proceedings of the 49th AIAA Aerospace Sciences Meeting Including the New Horizons Forum and Aerospace Exposition, Orlando, FL, USA, 4–7 January 2011; p. 1121.
15. Rajmohan, N.; Zhao, J.; He, C. A coupled vortex particle/CFD methodology for studying coaxial rotor configureurations. In Proceedings of the Fifth Decennial AHS Aeromechanics Specialists' Conference, San Francisco, CA, USA, 22–24 January 2014.
16. Lakshminarayan, V.K.; Baeder, J. High-resolution computational investigation of trimmed coaxial rotor aerodynamics in hover. *J. Am. Helicopter Soc.* **2009**, *54*, 42008. [CrossRef]

17. Hu, Z.; Xu, G.; Shi, Y. A robust overset assembly method for multiple overlapping bodies. *Int. J. Numer. Methods Fluids* **2021**, *93*, 653–682. [CrossRef]
18. Roget, B.; Sitaraman, J. Robust and efficient overset grid assembly for partitioned unstructured meshes. *J. Comput. Phys.* **2014**, *260*, 1–24. [CrossRef]
19. Farassat, F. Linear acoustic formulas for calculation of rotating blade noise. *AIAA J.* **1981**, *19*, 1122–1130. [CrossRef]
20. Yu, P.; Hu, Z.; Hu, J.; Xu, G.; Shi, Y. Numerical studies on the aeroelasticity of a shipboard helicopter rotor during engagement and disengagement with ship motions using CFD/CSD coupling approach. *Aerosp. Sci. Technol.* **2023**, *14*, 108559. [CrossRef]
21. Hu, Z.; Xu, G.; Shi, Y.; Xia, R. Airfoil–vortex interaction noise control mechanism based on active flap control. *J. Aerosp. Eng.* **2022**, *35*, 04021111. [CrossRef]
22. He, C.; Zhao, J. Modeling rotor wake dynamics with viscous vortex particle method. *AIAA J.* **2009**, *47*, 902–915. [CrossRef]
23. Yang, Y.; Xu, G.; Shi, Y. Research on a robust overset grid method for load calculation of coaxial rotor. *Int. J. Aeronaut. Space Sci.* **2022**, *23*, 484–500.
24. Cross, J.L.; Watts, M.E. *Tip Aerodynamics and Acoustics Test: A Report and Data Survey*; NASA: Washington, DC, USA, 1988.
25. Yu, Y.H.; Tung, C.; Gallman, J.; Schultz, K.J.; van der Wall, B.; Spiegel, P.; Michea, B. Aerodynamics and acoustics of rotor blade-vortex interactions. *J. Aircr.* **1995**, *32*, 970–977. [CrossRef]
26. Spalart, P.R.; Allmaras, S.R. A One-Equation Turbulence Model for Aerodynamic Flows. In Proceedings of the 30th Aerospace Sciences Meeting and Exhibit, AIAA Paper 1992-0439, Reno, NV, USA, 6–9 January 1992.
27. Kim, J.W.; Park, S.H.; Yu, Y.H. Euler and Navier-Stokes simulations of helicopter rotor blade in forward flight using an overlapped grid solver. In Proceedings of the 19th AIAA Computational Fluid Dynamics, San Antonio, TX, USA, 22–25 June 2009.
28. Strawn, R.C.; Duque, E.P.N.; Ahmad, J. Rotorcraft aeroacoustics computations with overset grid CFD methods. *J. Am. Helicopter Soc.* **1999**, *44*, 132–140. [CrossRef]
29. Wu, X. Aerodynamic Problems and Research Progresses of Rigid Coaxial Rotor. *J. Nanjing Univ. Aeronaut. Astronaut.* **2019**, *51*, 137–146.

Disclaimer/Publisher's Note: The statements, opinions and data contained in all publications are solely those of the individual author(s) and contributor(s) and not of MDPI and/or the editor(s). MDPI and/or the editor(s) disclaim responsibility for any injury to people or property resulting from any ideas, methods, instructions or products referred to in the content.